Tornadoes in Southeast South America: Mesoscale to Planetary-Scale Environments

DANIEL VELOSO-AGUILA,[a] KRISTEN L. RASMUSSEN,[a] AND ERIC D. MALONEY[a]

[a] *Department of Atmospheric Science, Colorado State University, Fort Collins, Colorado*

(Manuscript received 19 September 2022, in final form 1 November 2023, accepted 7 November 2023)

ABSTRACT: A multiscale analysis of the environment supporting tornadoes in southeast South America (SESA) was conducted based on a self-constructed database of 74 reports. Composites of environmental and convective parameters from ERA5 were generated relative to tornado events. The distribution of the reported tornadoes maximizes over the Argentine plains, while events are rare close to the Andes and south of Sierras de Córdoba. Events are relatively common in all seasons except in winter. Proximity environment evolution shows enhanced instability, deep-layer vertical wind shear, storm-relative helicity, reduced convective inhibition, and a lowered lifting condensation level before or during the development of tornadic storms in SESA. No consistent signal in low-level wind shear is seen during tornado occurrence. However, a curved hodograph with counterclockwise rotation is present. The Significant Tornado Parameter (STP) is also maximized prior to tornadogenesis, most strongly associated with enhanced CAPE. Differences in the convective environment between tornadoes in SESA and the U.S. Great Plains are discussed. On the synoptic scale, tornado events are associated with a strong anomalous trough crossing the southern Andes that triggers lee cyclogenesis, subsequently enhancing the South American low-level jet (SALLJ) that increases moisture advection to support deep convection. This synoptic trough also enhances vertical shear that, along with enhanced instability, sustains organized convection capable of producing tornadic storms. At planetary scales, the tornadic environment is modulated by Rossby wave trains that appear to be forced by convection near northern Australia. Madden–Julian oscillation phase 3 preferentially occurs 1–2 weeks ahead of tornado occurrence.

SIGNIFICANCE STATEMENT: The main goal of this study is to describe what atmospheric conditions (from local to global scales) are present prior to and during tornadic storms impacting southeast South America (SESA). Increasing potential for deep convection, wind shear, and potential for rotating updrafts, as well as reducing convective inhibition and cloud-base height, are predominant a few hours before and during the events in connection to low-level northerly winds enhancing moisture transport to the region. Remote convective activity near northern Australia appears to influence large-scale atmospheric circulation that subsequently triggers convective storms supporting tornadogenesis 1–2 weeks later in SESA. Our findings highlight the importance of accounting for atmospheric processes occurring at different scales to understand and predict tornado occurrences.

KEYWORDS: South America; Large-scale motions; Storm environments; Tornadoes; Mesoscale processes; Reanalysis data

1. Introduction

Severe thunderstorms cause extensive damage to property and devastating loss of human life. The exposure to severe storms has substantially increased during the last few decades and is expected to continue rising in the future. Among the main reasons explaining this are changes in population dynamics and extreme weather events caused by climate change (Tuholske et al. 2021; Swain et al. 2020; Yang et al. 2019), which are increasing monetary losses (Bouwer 2019) and disaster risk (IPCC 2012) worldwide. Tornadic storms have been extensively studied in the United States, where robust observing networks and advances in numerical weather prediction models allow tornado threats to be anticipated with reasonable accuracy (Brotzge and Donner 2013; Brooks and Correia 2018). Other regions such as South America do not have dense observational networks (including vertical soundings and ground-based radars) nor routine collection and archiving of severe weather reports, contributing to a lack of studies about and limiting advanced warning of these life-threatening events (Nascimento and Doswell 2006).

South America is prone to some of the most intense severe thunderstorms globally (Zipser et al. 2006; Cecil and Blankenship 2012; Houze et al. 2015), including tornadoes (Goliger and Milford 1998; Brooks et al. 2003). The environments that support the formation of tornadoes are generally located east of major mountain ranges (e.g., the Rockies and the Andes), where severe weather conditions are frequent during the warm season (Zipser et al. 2006; Houze et al. 2015). In southeast South America (SESA), conditions favoring severe weather are supported by a poleward-extended low-level jet [i.e., South American low-level jet (SALLJ; Vera et al. 2006; Montini et al. 2019; Sasaki et al. 2022)], often enhanced by a synoptic trough, which helps to destabilize the environment by advecting warm and humid air from the Amazon basin (Rasmussen and Houze 2016). Dry westerly flow crossing the mountains can override this low-level meridional moisture flux, creating steep midlevel lapse rates (Banacos and Ekster 2010;

Corresponding author: Daniel Veloso-Aguila, dan.veloso_aguila@colostate.edu

DOI: 10.1175/MWR-D-22-0248.1

Ribeiro and Bosart 2018), with a capping inversion downstream that prevents widespread convection (Rasmussen and Houze 2011, 2016). The synoptic forcing also produces strong midlevel vertical wind shear (Piersante et al. 2021), a key ingredient for mesoscale convective systems (MCSs) that are often initiated along the foothills of the Andes and the Sierras de Córdoba (hereafter SDC) that help to overcome the capping.

Tornadoes have been frequently observed in SESA (Schwarzkopf 1988; Nunes et al. 2011; Silva Dias 2011; Rasmussen et al. 2014), but it is difficult to determine how frequent they are relative to other regions of the world, as the reporting procedures are different, the observational network in SESA is very sparse, and early estimates are likely biased by low reporting numbers in low-population regions [e.g., throughout the Pampas of Argentina (Potvin et al. 2022)]. Tornado occurrence in SESA is assumed to be lower than in the United States, where the number of reports is typically over 1000 yr^{-1} (https://www.ncdc.noaa.gov/societal-impacts/tornadoes/), even though the U.S. tornado reports have increased over time due to greater population growth, installation of a dense radar network beginning in the 1980s, and other factors (Nouri et al. 2021; Potvin et al. 2022). In terms of tornado environments, Brooks et al. (2003) used the ingredients that support significant tornado events in the United States to estimate tornado frequency across the globe based on reanalysis data. Their findings suggest that tornadoes over SESA are less frequent than in the United States, although extrapolating the same parameters that favor tornadic storms in the United States to South America may be a poor assumption due to differences in environmental forcing and topography, among other factors. A more detailed and modern study of mesoscale through planetary-scale environments supporting the occurrence of tornadic storms is necessary for improved understanding of severe weather in this region. In this context, the emergence of novel reanalysis products such as ERA5 (Hersbach et al. 2020) have been useful in representing convective environments associated with tornadoes in the United States and Europe with high accuracy (Taszarek et al. 2020, 2021; Coffer et al. 2020; Varga and Breuer 2022), and may prove similarly useful for SESA.

Numerous tornado case studies for South America have been conducted, including Brazil (Lima 1982; Oliveira 2004; Nascimento et al. 2014; Rehbein et al. 2018; Pereira Filho et al. 2019; Lopes and Nascimento 2020; Oliveira et al. 2022); Argentina (Schwarzkopf and Rosso 1993; Natalini et al. 2012; Pita and Schwarzkopf 2016); Uruguay (DNM 2002; Durañona 2016; http://tornadoseneluruguay.blogspot.com/); Colombia (Ortiz-Royero and Rosales 2012); and Chile (Barrett et al. 2020; Vicencio et al. 2021). However, very few studies have focused on climatological aspects of tornado reports and their intensities (Schwarzkopf 1988; Nunes et al. 2011; Silva Dias 2011; Rasmussen et al. 2014; Lopes 2020; dos Santos et al. 2023), and virtually no studies exist on the environments supporting tornadic storms. Schwarzkopf (1988) conducted the first effort in materializing a tornado database in SESA by compiling hundreds of carefully identified reports between 1930 and 1987. More recently, through local newspapers, Rasmussen et al. (2014) compiled several tornado storm reports that occurred in central and northeastern Argentina since 1997 and were observed by the TRMM satellite's Precipitation Radar. Further efforts from local scientists have made it possible to compile historical reports of tornadoes in Brazil (Nunes et al. 2011; Silva Dias 2011; dos Santos et al. 2023) and Chile (Vicencio et al. 2021), including analysis of tornado distribution and intensity. Vicencio et al. (2021) found that an extended period of postfrontal activity with modest instability (<1000 J kg^{-1}) and strong low- and midlevel shear was instrumental for a cold-season tornado outbreak in Chile. Beyond these limited efforts, there are no formal studies specifically addressing the general environment supportive of tornadoes using an ingredients-based approach (Doswell et al. 1996) for severe thunderstorms in SESA.

Teleconnections associated with large-scale modes of variability such as El Niño–Southern Oscillation (ENSO) and the Madden–Julian oscillation (MJO) can also affect the local conditions that support severe weather. For example, the Pacific–South America (PSA) teleconnection pattern can be modulated by ENSO that affects the strength of the SALLJ and associated mesoscale convective systems (e.g., Silva and Ambrizzi 2006; Montini et al. 2019). Changes in extreme precipitation and the characteristics of convection in SESA have been documented through such ENSO teleconnections (e.g., Grimm and Tedeschi 2009; Bruick et al. 2019). The MJO can similarly excite extratropical teleconnections that modulate circulations and precipitation in South America (Carvalho et al. 2004; Alvarez et al. 2016). Teleconnections from the tropics associated with phenomena like ENSO and the MJO have been extensively documented to modulate severe weather and tornadoes over North America (e.g., Tippett 2018; Thompson and Roundy 2013; Baggett et al. 2018), but little work has been done in South America (e.g., Barrett et al. 2020).

A key objective of this study is to determine what environmental conditions support tornadoes in SESA at various scales, contrasting with tornadoes in the United States given the apparent differences in frequency between these two regions. We will address the following questions: What dynamic or thermodynamic parameters are important for tornadogenesis in SESA at the mesoscale? What synoptic conditions favor the formation of tornadoes in SESA? How important is planetary-scale forcing for modulating tornadic storms with implications for predicting their occurrence in SESA? Are there any tropical sources of predictability for tornadic storms in SESA? To address these questions, section 2 will describe the data and methods used to describe the tornadic environment over SESA using a compendium of tornado reports in the region; section 3 will examine tornado distributions and storm-mode characteristics; section 4 will address the mesoscale environment supporting tornadoes and discussion of differences and similarities between the environments supporting tornadic storms in SESA and the United States; section 5 will address synoptic- and planetary-scale forcing (including teleconnections) modulating the environment conducive to tornadic storms. Finally, section 6 will present the main conclusions of the study.

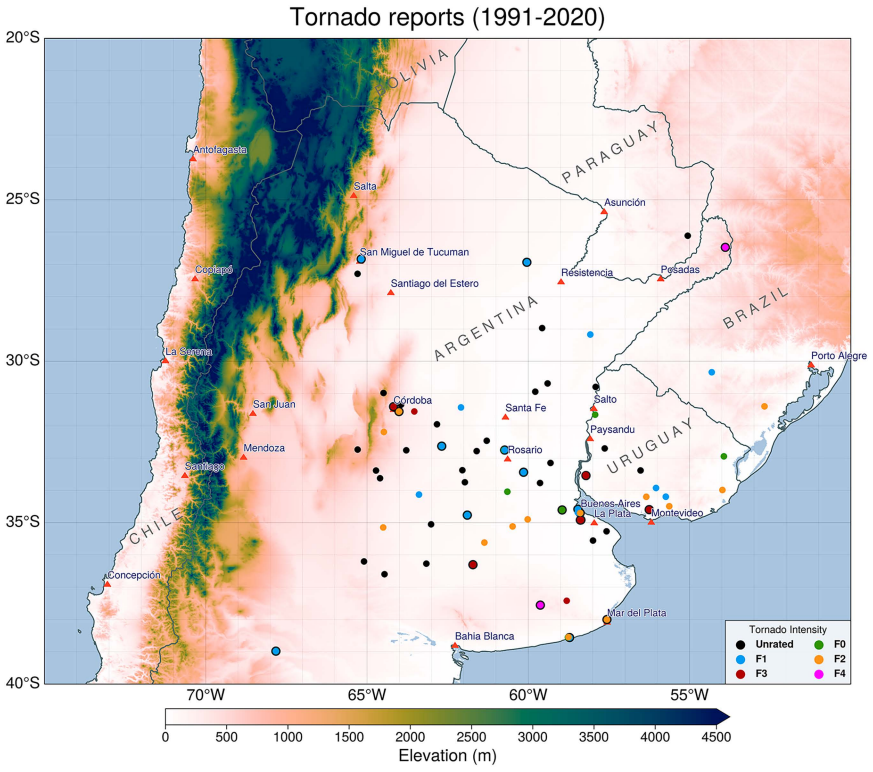

FIG. 1. Selected tornado reports collected over subtropical South America ($N = 74$). Color in dots represents estimated tornado intensity on the F-scale. Cases whose intensity was confirmed have a thick black edge. Terrain elevation (m) is shown in shading. A red triangle indicates the location of selected cities.

2. Methodology

a. Tornado event climatology

Given that no official severe weather report database (including tornadoes) exists in South America, we performed a full search of digital newspaper archives, social media, and other online sources to create a database of tornadic events in subtropical South America after 1991. This effort resulted in a compendium of 74 tornadic events spanning Argentina, Paraguay, Uruguay, and southern Brazil, between 1991 and 2020 (Veloso-Aguila 2023). Most of the reports are from Argentina and Uruguay, as can be seen in Fig. 1. It is important to note that not all the reports we use experience the same rigorous quality control that is conducted within the United States, for example, by the National Weather Service. Most of the reports were collected from an anonymous online repository that assembled confirmed and unconfirmed events in Argentina, Brazil, Paraguay, and Uruguay, using the *Google My Maps* Application (https://www.google.com/maps/d/viewer?mid=1E_a0e2B9ftXNQ-F5XIZgnGps2So&usp=sharing). Nonetheless, supporting details were needed due to the lack of evidence to validate many of these reports. Thus, numerous events were confirmed by using information about tornado events shared by meteorology enthusiasts (who occasionally included data from radar and satellite imagery) in an online meteorology forum (http://foro.gustfront.com.ar/). Individual efforts from meteorologists who gathered evidence (pictures and videos) and visited the damaged area to confirm the occurrence of a tornado in a specific location, and shared the information in personal blogs (e.g., http://tornadoseneluruguay.blogspot.com/), were also included. Clock changes due to daylight saving time and other factors across the South American countries were also considered to preserve correct conversion to UTC when required. A table with detailed information on every tornado event used in this study is found in Veloso-Aguila (2023), including online sources of information that confirm the occurrence of every single case, approximate location, any available intensity information, and time of occurrence.

It is important to point out that the actual number of reports collected for the present study was much higher. However, the lack of information such as the time of occurrence that is required to conduct hourly analysis, approximate location of the event, or strong visual evidence of the funnel cloud or the damage caused required to label the event as a tornado (e.g., local people sometimes confuse a tornado with strong straight-line winds) prevented us from building a larger database. Due to time constraints, we were also not able to explore all tornado events in southern Brazil, so we only included two of the dozens of potential reports in our database. Consequently, we do not accurately represent the tornado environment in southern Brazil, but the reader can

refer to Silva Dias (2011) or Lopes (2020) for further information over that region. Another aspect that reduced the total number of reports was that we only selected a single report within an outbreak to provide equal weighting to environmental conditions when composites were calculated. As a result, the distribution of the events shown in Fig. 1 may not be representative of the actual density of tornadoes in SESA.

b. *ERA5*

Hourly ERA5 data (Hersbach et al. 2020) are used to characterize the mesoscale and large-scale environments associated with the tornado events. ERA5 is the fifth-generation reanalysis product from ECMWF, covering the period 1979–2021 with 0.25° × 0.25° horizontal grid spacing. Composite anomalies of the synoptic and large-scale environments supporting tornadic storms are calculated using data on single levels (e.g., vertically integrated or surface fields) and pressure levels (upper-air fields). Differences relative to the long-term means are used to calculate daily anomalies based on the climatological period of 1991–2020, the same period of the reported tornadoes used here. In addition, model-level ERA5 data were employed, which has a higher vertical resolution (137 versus 37 levels) and terrain-following coordinates, thus allowing a more precise calculation of some convective parameters. Proximity soundings were obtained using the closest ERA5 grid point to every tornado report at the closest time and time-evolution composites spanning 24 h before and after the event were obtained by applying the same approach. A sensitivity test of the results to be presented in section 4 that considered the average of the closest 25 grid points to every tornado as the proximity sounding showed negligible differences with the closest gridpoint approach (not shown). Around 10% of the proximity soundings at the closest time of tornado occurrence show some evidence of potential convective contamination (e.g., cold pool sampling or deep saturated layer). Composite analyses removing those cases show a significant, but small impact overall. Hence, given the small sample of tornado events collected over SESA, all events are retained for the analyses conducted in section 4. It is worth noting that ERA5 fields are strongly influenced by the model used to generate the reanalysis, especially in data-sparse regions away from sounding sites. Hence, we acknowledge that the representation of the tornadic environment may be strongly influenced by the physical parameterizations in the reanalysis model.

TORNADIC PARAMETERS

An assortment of severe weather parameters that are normally used to study tornadic environments are analyzed in this research:

- Mixed-layer convective available potential energy (MLCAPE, J kg^{-1}): the potential energy of the atmosphere to produce free convection and unforced air ascent. Unlike typical estimates of surface-based CAPE (where the air parcel initially holds the near-surface conditions), MLCAPE considers an air parcel starting with the mean conditions in the lowest 100 hPa. As a result, it accounts better for the atmospheric conditions in the boundary layer. MLCAPE has been widely used to explore tornadic environments (Brooks et al. 2003; Brooks 2009; Grams et al. 2012; Thompson et al. 2012; Anderson-Frey et al. 2016; Taszarek et al. 2020). High MLCAPE (>1000 J kg^{-1}) is often required to trigger deep convective clouds, though low CAPE environments (<500 J kg^{-1}) can also support severe thunderstorms (Guyer and Dean 2010; Davis and Parker 2014; Sherburn and Parker 2014).
- Mixed-layer convective inhibition (MLCIN; J kg^{-1}): the amount of energy that an air parcel needs to overcome while negatively buoyant in order to reach the level of free convection. Moderate CIN can allow convection to be severe instead of widespread and short-lived by allowing convective instability to build over time. However, if CIN is too strong, convection may not occur if a suitable lifting mechanism cannot overcome the negative buoyancy.
- Mean-layer lifting condensation level (MLLCL; m): the height level at which an ascending parcel becomes saturated, based on a surface temperature and dewpoint calculated from the mean profile in the lowest 100 hPa. High relative humidity at low levels causes rising air parcels to reach saturation at lower elevations. Evidence shows that the mean-layer technique is more suitable for studies of convective processes in the atmosphere instead of that using a surface-based parcel (e.g., Craven et al. 2002). Tornadogenesis is more likely when no strong cold pools develop that suppress the updraft, and hence a low cloud-base height is present. Evaporative cooling that induces cold pools is controlled by the moisture content (i.e., relative humidity) at low-levels, meaning that a humid layer will prevent raindrops from evaporating, thus enabling updrafts to grow.
- Bulk vertical wind shear (BSH; m s^{-1}): the surface to height above ground level change in wind, calculated over the lowest 1-km (BSH01) and 6-km (BSH06) layer above ground level. We use the wind difference between the respective layer limits. Deep-layer shear is important to the organization and longevity of storms (e.g., supercells or MCSs), while high low-level shear environments tend to favor tornadic storms by enhancing the updraft and vertical vorticity at low levels (Coffer and Parker 2015).
- Storm-relative helicity (SRH; m^2 s^{-2}): the potential for a cyclonic updraft in a storm (i.e., potential for supercellular, rotating storms), is calculated over the 0–1-km (SRH01) and 0–3-km (SRH03) layers above ground level. To estimate the storm-relative winds, we use the Bunkers storm motion vector in the Southern Hemisphere, i.e., left-moving supercell (Bunkers et al. 2014), thus making SRH normally negative. Low-level SRH is particularly helpful to assess tornadogenesis potential of a storm (Coffer et al. 2019).
- Significant tornado parameter (STP): a parameter composed of multiple variables relevant to tornadogenesis, is calculated by combining the values from multiple convective parameters to obtain a single value. The effective inflow layer is considered for SRH and BSH computations (ESRH and EBSH), and the lowest 100 mb mixed-layer for CAPE, CIN, and LCL (MLCAPE, MLCIN, and MLLCL) [see Thompson et al. (2004) for further details in its computation]. STP values are greater (lower) or equal to zero in

the Northern (Southern) Hemisphere, based on positive (negative) SRH input. STP greater than 1 in magnitude appears to indicate higher chances for significant tornadic supercells in lieu of nontornadic supercells (Thompson et al. 2003).

The following convective parameters were computed using the *SharpPy* Python library (Blumberg et al. 2017): MLCAPE, MLCIN, MLLCL, BSH, SRH, and STP.

c. *International Satellite Cloud Climatology Project (ISCCP)*

Given the lack of observational data in the region and to provide insights about the storm size accompanying every tornadic event, cloud-top temperatures for clouds detected by IR threshold brightness temperatures (Tc) from the HGG (H-series Gridded Global) ISCCP–Basic H-Series product were used (Young et al. 2018). The ISCCP product has a $1° \times 1°$ equal-angle horizontal spacing and 3-h temporal resolution and extends from July 1983 through June 2017. To estimate the cloud shield size for every event to discriminate between small isolated and large convective systems, a threshold of Tc = −48°C is used. The convective feature that is closest to the tornadic event in time and space is taken into account by adding all the pixels having Tc < −48°C that are connected. If the tornado is not collocated with the convective feature, we consider the closest feature associated to the tornado. In this way, a broad perspective on whether tornadoes in subtropical South America are produced by isolated supercells or are embedded into larger and organized MCSs is possible. Note that modest inaccuracies in the estimation of the cloud shields sizes caused by different satellite view zenith angles are possible (Knapp et al. 2021). Given the period of this data (ending in July 2017), only 66 events are considered for the comparison with satellite fields, with an additional 4 of them subsequently removed due to inconsistencies between the convective feature shown by the satellite product and the approximate location and time of the tornado. Among the potential reasons for the mismatch are errors in the tornado location, errors in tornado time of occurrence, very short-lived convective cells not captured by the 3-hourly data, or unknown errors in the ISCCP dataset caused by steep satellite view zenith angles.

d. *NOAA outgoing longwave radiation (OLR) and Madden–Julian oscillation (MJO)*

To give an idea of potential sources of teleconnections originating from the tropics that modulate the large-scale conditions affecting tornado-producing storms in SESA, the daily NOAA OLR product (Liebmann and Smith 1996) is used. This product is on a regular $1° \times 1°$ grid and is available from 1974 to 2021. To further explore the contribution of tropical subseasonal variability to SESA tornado activity, an analysis of the MJO and its relationship with the tornadic environment is performed using the Real-time multivariate MJO index (RMM) (Wheeler and Hendon 2004). We assess the phase of the MJO 1–2 weeks in advance of every tornadic event for any active MJO day (RMM amplitude > 1) to determine if preferred MJO phases are associated with tornadogenesis.

3. Tornadic storm characteristics

a. *Tornado storm report database*

The location of every tornado storm report identified in Argentina, Uruguay, and southern Brazil in this study is illustrated in Fig. 1. According to the map, most of the reports are concentrated between 30° and 40°S, in the area with the lowest elevations in the region to the east of the Andes mountains. However, there are many reports tied to small topographic features such as east of the SDC (e.g., in Córdoba). Although very uncommon, a couple of tornadic events also occurred in the Andes foothills in northwestern Argentina. Some areas have a higher concentration of events (e.g., Buenos Aires and Córdoba metropolitan areas), likely because of the denser population over these locations compared to other parts of SESA that enhances the chances of experiencing and reporting a tornadic event (e.g., Anderson et al. 2007; Ray et al. 2003). Information about tornado intensity—when available—is also included on the map. About 60% of the cases do have some report about intensity in the F-scale (Fujita 1971), but only 40% of them (18 events) have been confirmed (i.e., intensity has been verified), either by peer review studies (e.g., Pita and Schwarzkopf 2016), independent investigations conducted by meteorologists or scientists (e.g., http://tornadoseneluruguay.blogspot.com/), or official reports issued by the weather service or related organizations. The F-scale ratings collected here may not follow same quality standards of, for instance, the U.S. National Weather Service, though. The most frequent tornado intensities reported are F1 and F2, and a few confirmed F3 and F4 tornadoes are also included. For the remaining 40% of the events, reliable evidence to label them with any intensity category was not found. There is evidence of a few F5 tornadoes happening in SESA prior to 1990, but they are beyond the study period (Schwarzkopf 1988).

The temporal distribution of tornadic storm reports (Fig. 2a) shows that the majority tend to happen during the extended warm season (October–April), with few reports during the cold season (May–September). December is the month with the highest frequency of reports, while tornadoes in June and July are the least frequent. February has the lowest number of reports within the extended warm season. The annual cycle distribution is generally like that in Schwarzkopf (1988), although they found January to have the highest number of tornado reports. This distribution shows that tornadoes in SESA occur not only in spring and summer, but also during fall, which reinforces the findings from Zipser et al. (2006) who showed frequent intense thunderstorms happening in SESA in almost all the seasons.

Analysis of the diurnal cycle of tornadic events from Fig. 1 reveals a bimodal distribution (Fig. 2b). Most of the events occur during the local afternoon hours, peaking around 1600–1700 LT, and decreasing in frequency through the early night. A secondary and lower peak in frequency occurs between late night and early morning. The morning hours (0800–1200 LT) showed the fewest number of reports. This distribution may not necessarily represent the actual diurnal cycle of tornado frequency in SESA. The database used does not include many reported tornadoes in southern Brazil,

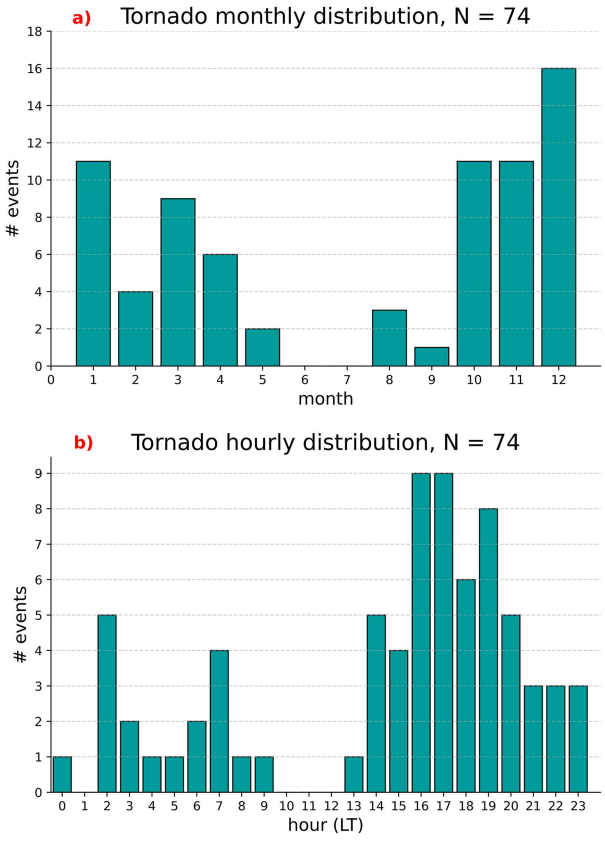

FIG. 2. Distribution of the 74 tornadoes collected between 1991 and 2020 for the present study by (top) month of the year and (bottom) hour of the day (local time).

where nocturnal tornadoes might be more frequent. Besides, a bias toward more reports during daytime is expected due to reduced visibility and fewer people witnessing events during the night in a region with weak radar coverage (Trapp et al. 2006).

b. *Storm size distribution*

Figure 3 shows the size distribution of the cloud shields associated with the storms producing the tornadoes (please refer to section 2c for details in the storm size estimation). 49 storms had a cloud shield that was ≥1 pixel (~10 000 km^2), while 13 of the remaining cases did not meet the criteria, either because the storm was deep but smaller than the 10 000 km^2 needed to be captured on a 1° × 1° grid box, or the cloud top was not cold enough, which can be the case for low-topped supercells (Kennedy et al. 1993). To get insights into the estimated size and strength of cells for these 13 cases, the high resolution (0.1° grid spacing) ISCCP H-series pixel-level global product (HXG) (Young et al. 2018) was examined, including a visual inspection of satellite imagery from the Global ISCCP B1 Browse System (GIBBS) (accessible here: https://www.ncdc.noaa.gov/gibbs/). For the remaining four cases it was not possible to connect the location of the tornado to a cloud shield, likely because of the lack of a convective feature close enough

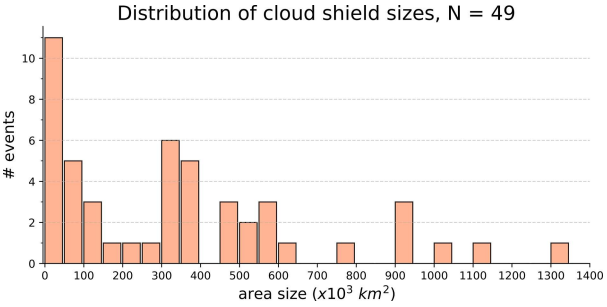

FIG. 3. Histogram of estimated cloud shield size from 49 tornadic storms using an ISCCP cloud-top temperature threshold of −48°C. Cases whose size is estimated to be small enough to be captured by the ISCCP gridded data are not included here. See text for details.

to the tornado, as determined using the multiple approaches mentioned above (not shown). The lack of higher temporal resolution data may also cause a mismatch between the tornado location and the convective feature. Tornadoes mismatched by more than one hour from the satellite data may miss the evolution and location of fast-evolving storms. For events that occurred in between two snapshots (e.g., tornado reported at 1330 LT and the closest imagery occurring at 1200 and 1500 LT), we assigned the average storm size from the convective feature located over the tornado as the average of both times. Therefore, the ultimate analysis performed in this section is based on 62 tornadic storms from January 1991 to June 2017.

The distribution of storm sizes presented in Fig. 3 shows a large spread in the cloud shield size, where storms can be less than 50 000 km^2 or be as big as 1 300 000 km^2, though most of them concentrate below 650 000 km^2. Given that MCSs are considered to have scales of hundreds of kilometers in diameter (Houze 2004; Schumacher and Rasmussen 2020), at least 30 tornadoes appear to be embedded into MCS-like storms (>150 000 km^2). Yet, this does not necessarily mean that tornadoes are being produced mostly by MCSs (e.g., squall lines); tornado-producing supercells may be located close to large convective systems showing large cloud shield signals that potentially disguise independent isolated cells. On the other hand, around 13 events with sizes below the data resolution (and thus cannot be shown in Fig. 3) may be supercell tornadoes or landspouts given their characteristic smaller sizes. Additionally, a comparison of the time of occurrence of tornadoes and the corresponding cloud shield size shows that nocturnal tornadoes are associated with 20% larger cloud shields than daytime events. This may be due to convective systems that initiate in the afternoon and grow upscale through the night, a process frequently observed in this region (Mulholland et al. 2018, 2019; Piersante et al. 2021; Rasmussen and Houze 2011, 2016; Rasmussen et al. 2014, 2016). A general outcome from Fig. 3 and the additional 13 cases examined is that tornadic storms more frequently develop from isolated thunderstorms or small MCSs rather than large convective systems, which broadly agrees with the predominance of discrete and embedded supercell tornadic storms over other

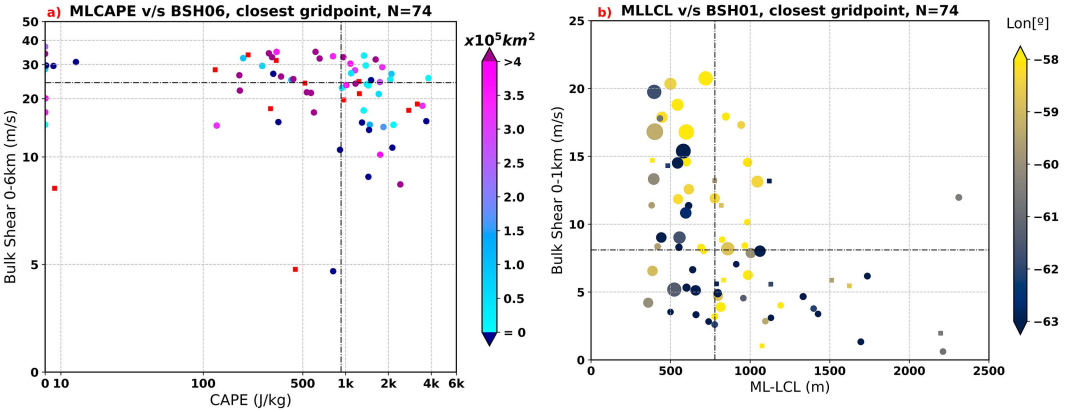

FIG. 4. Scatterplot for the 74 tornadoes, using the closest grid point at the closest time to the respective event. (a) MLCAPE vs BSH06; color bar indicates the size of the cloud shield (size below 1pixel in dark blue and over 40 pixels in dark magenta). (b) MLLCL vs BSH01; color bar indicates the location of the event in longitude and the marker size represents the size of the cloud shield. Red squares in (a) and colored squares in (b) indicate events happening after June 2017, when ISCCP data to estimate storm sizes were not available. Dashed lines show the median value for the corresponding parameter.

storm modes observed in the U.S. Great Plains (Smith et al. 2012).

4. Mesoscale environments supporting tornadic storms

a. *Mesoscale proximity environments*

ERA5 is used to analyze the mesoscale ingredients that support tornadic storms in SESA. Figure 4a presents the distribution of the MLCAPE and BSH06 environment at the closest times and gridpoint locations to the tornado events. From research on U.S. convective storms, it is well known that large CAPE and deep-layer shear values are favorable for producing severe weather, including tornadoes (Rasmussen and Blanchard 1998; Brooks et al. 2003; Grams et al. 2012; Thompson et al. 2012) and organized convective storm modes (Jorgensen and Weckwerth 2003). In our tornado event database, there is a concentration of events showing moderate to high MLCAPE and high BSH06 values; the median of the distribution is located at 929 J kg^{-1} for MLCAPE and 24 m s^{-1} for BSH06. Around 2/3 of the cases present high wind shear values (>20 m s^{-1}) and ~38% a highly unstable environment (MLCAPE > 1250 J kg^{-1}). Only 3% of the tornadic storms are positioned in the low-shear, low-CAPE quadrant (<10 m s^{-1} and <500 J kg^{-1}, respectively). When compared to the typical U.S. tornado environment, the CAPE versus BSH06 scatterplot in Fig. 4a broadly agrees with that shown by Brooks et al. (2003) and Anderson-Frey et al. (2016) for tornado events over the United States in terms of the maximum density location. Additionally, some events presenting MLCAPE < 10 J kg^{-1} (~12% of all cases) can be observed; potential caveats in the reanalysis product (errors in representing boundary layer structure due to limited observations in SESA and insufficient spatial resolution and/or time stepping) could explain these numbers. Indeed, most of these events had moderate to large MLCAPE values a few grid points/hours displaced from the tornado event (not shown). High-shear, high-CAPE environments are more likely to support large and organized MCSs in U.S. storms (Jorgensen and Weckwerth 2003). Storms with cloud shield sizes of 400 000 km^2 or more (i.e., very large MCSs) are also mostly concentrated in the high-shear, high-CAPE environment (Fig. 4a) in our analysis.

Although CAPE and BSH06 are relevant for severe weather production, boundary layer relative humidity (i.e., cloud-base height), and low-level wind shear have been shown to be among the two most important factors in discriminating between nontornadic and tornadic storms (Thompson et al. 2012; Markowski et al. 2003; Brooks and Craven 2002). Figure 4b shows the MLLCL versus BSH01 environment from the 74 tornadic events over SESA. For tornadoes having large BSH01 values, MLLCL is small, and vice versa. For instance, when BSH01 > 15 m s^{-1}, MLLCL is below 950 m, and when MLLCL > 1300 m, BSH01 values exceed 6.5 m s^{-1} in 1 out of 10 events. The median values for MLLCL and BSH01 for the 74 events are 778 m and 8.1 m s^{-1}, respectively. MLLCL is on the order of that observed for significant tornadic storms in the United States, although BSH01 is moderate to weak as it is within the lowest 25% of the BSH01 distribution for U.S. tornadoes (Thompson et al. 2003, 2012). The MLLCL versus BSH01 environment in Fig. 4b more closely resembles the significant severe scatterplot shown in Brooks et al. (2003) than the significant tornado scatterplot, with the latter presenting higher BSH01 values overall. Additionally, Fig. 4b shows the longitudinal location and storm size in relation to the MLLCL versus BSH01 environment under which the tornado events occur. Although the behavior is complex, there is a suggestion that strong low-level shear is more likely when events occur far from the Andes and the storms are relatively large, while a weak shear environment is more frequent for events near the Andes and the SDC with smaller cloud shield sizes. One hypothesis for this behavior is that the extreme Andes elevation and very steep sloping cause low-level winds to be weak while the frequent strong synoptic forcing

explains the strong midlevel shear seen in observations from RELAMPAGO (Sasaki et al. 2022; Piersante et al. 2021). In terrain-modification modeling WRF experiments that varied the height of the Andes, Rasmussen and Houze (2016) showed that when reducing the Andes by 50%, the strength of the SALLJ reduced almost in half and also was shallower in vertical extent. Sasaki et al. (2022) showed that the SALLJ jet height was higher for strongly forced synoptic environments compared to the lower SALLJ heights for weakly forced synoptic environments. According to Fig. 4b, this influence in the low levels seems to diminish farther away from the Andes in eastern subtropical South America. On the other hand, frequent upscale growth over SESA (Rasmussen and Houze 2011; Rasmussen et al. 2016; Mulholland et al. 2018) may explain the tendency to get broader cloud shield tendency farther east. Future research with better observations of tornadic storm environments could investigate the variability in SALLJ depth and strength and its influence on the generation of low-level shear necessary for tornadogenesis, as well as the spatial variability on tornado storm mode, and the role of the Andes in these dynamic processes over SESA.

To explore the characteristic vertical profile of winds for tornadic storms in SESA, a composite hodograph based on the vertical wind profile from the closest grid point to every tornado is computed (Fig. 5). Counterclockwise rotation (backing in the Southern Hemisphere) is clear in most of the individual profiles and in the composite, especially at low levels, where NNE winds near the surface turn mostly westerly after reaching 2 km. This curved hodograph is broadly consistent with the veering structure for tornadic storms in the U.S. Great Plains, although the intensity and rotation are weaker at low levels in the SESA composite (the trajectory is already westerly by 1 km for U.S. tornadoes) (Maddox 1976; Markowski et al. 2003; Coffer and Parker 2015), which might be related to the taller Andes blocking westerly winds at higher levels. As a matter of fact, the core of the SALLJ has been observed at higher levels than its counterpart in the United States (Montini et al. 2019; Piersante et al. 2021; Sasaki et al. 2022). The hodograph is also consistent with the wind profile found by Rasmussen and Houze (2011) for storms having radar echoes with wide convective cores in SESA, which supports the supercellular or early maturing MCS storm structure prevalent in Fig. 3. The speed change with height agrees with the median values shown previously in Fig. 4. In the 3–6-km layer, a small veering in winds occurs that is likely not significant due to the low sample size, but consistent with hodograph composites for U.S. tornadic storms (Maddox 1976; Markowski et al. 2003). The spread of the individual hodographs is small near the surface as winds are weak, while near the tropopause the spread is large due to different pathways taken along the 12-km layer. Tropopause winds tend to favor the WSW direction, however.

Analysis of the composite time evolution of different tornadic parameters before and after the reported SESA tornado is presented in Fig. 6. These results will be contrasted with climatological studies done in the United States for tornadoes from different storm modes by Thompson et al. (2012) (hereafter T12) using the Rapid Update Cycle (RUC, currently

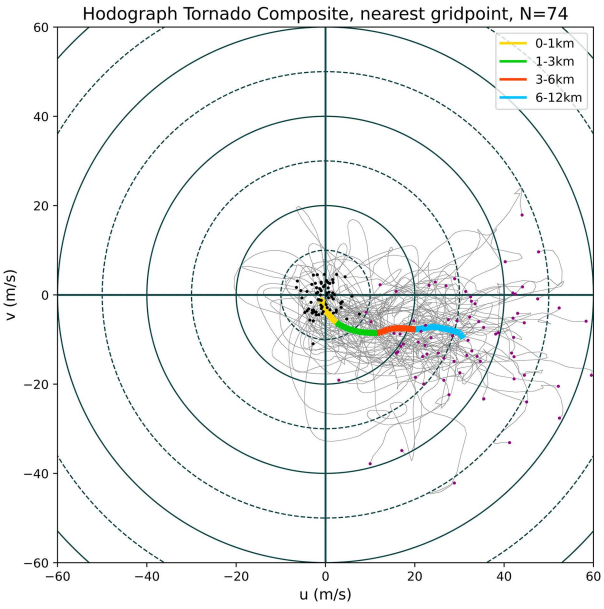

FIG. 5. Hodograph representing the 74 tornadoes (gray lines) and the mean circulation (thick colored line). Black (magenta) dots indicate the starting (ending) point of every hodograph at 10 m (12 km). Color-segmented lines indicate different layers. The closest grid point at the closest time to every event was used to get the wind profiles.

Rapid Refresh, RAP) model and analysis system, and tornadoes with various intensities (F-scale) by Taszarek et al. (2020) (hereafter T20) using ERA5. As expected, an unstable atmosphere is important for tornadic storm evolution (Fig. 6a), with MLCAPE starting to increase 24 h before the tornado is observed, followed by a steeper increase during the immediately preceding 10 h. Maximum average MLCAPE around 1250 J kg^{-1} is reached 2 h before the tornado (median MLCAPE $\sim$ 1140 J kg^{-1} at that time), followed by a sharp decrease, which reflects the importance of this parameter in building a robust storm that can spawn a tornado. The median MLCAPE during tornado occurrence (929 J kg^{-1}) is slightly weaker than MLCAPE values found in T12 for MCS or hybrid tornadoes but consistent with F0–F3 tornadoes in T20. Average MLCIN evolution (Fig. 6b) is somewhat noisy. High values (~ -110 J kg^{-1}) 24 to 14 h before the tornado, followed by stronger inhibition (~ -125 J kg^{-1}) 12 to 6 h before tornadogenesis, are consistent with what is normally seen prior to severe weather phenomena (Emanuel 1994). From -6 to -1 h, MLCIN decreases by $\sim$55 J kg^{-1}, reaching a minimum of ~ -70 J kg^{-1} on average at -1 h. The MLCIN observed at 0 h (median of ~ -65 J kg^{-1}) is slightly larger in magnitude than the values observed for tornadoes in the United States (T12; T20), suggesting a stronger resistance to widespread convection over SESA during tornadogenesis. Rasmussen and Houze (2016) showed that CIN is usually stronger in subtropical South America in comparison to the U.S. Great Plains due to a topographic enhancement caused by the higher elevation of the Andes, thus impacting the storm-mode characteristics.

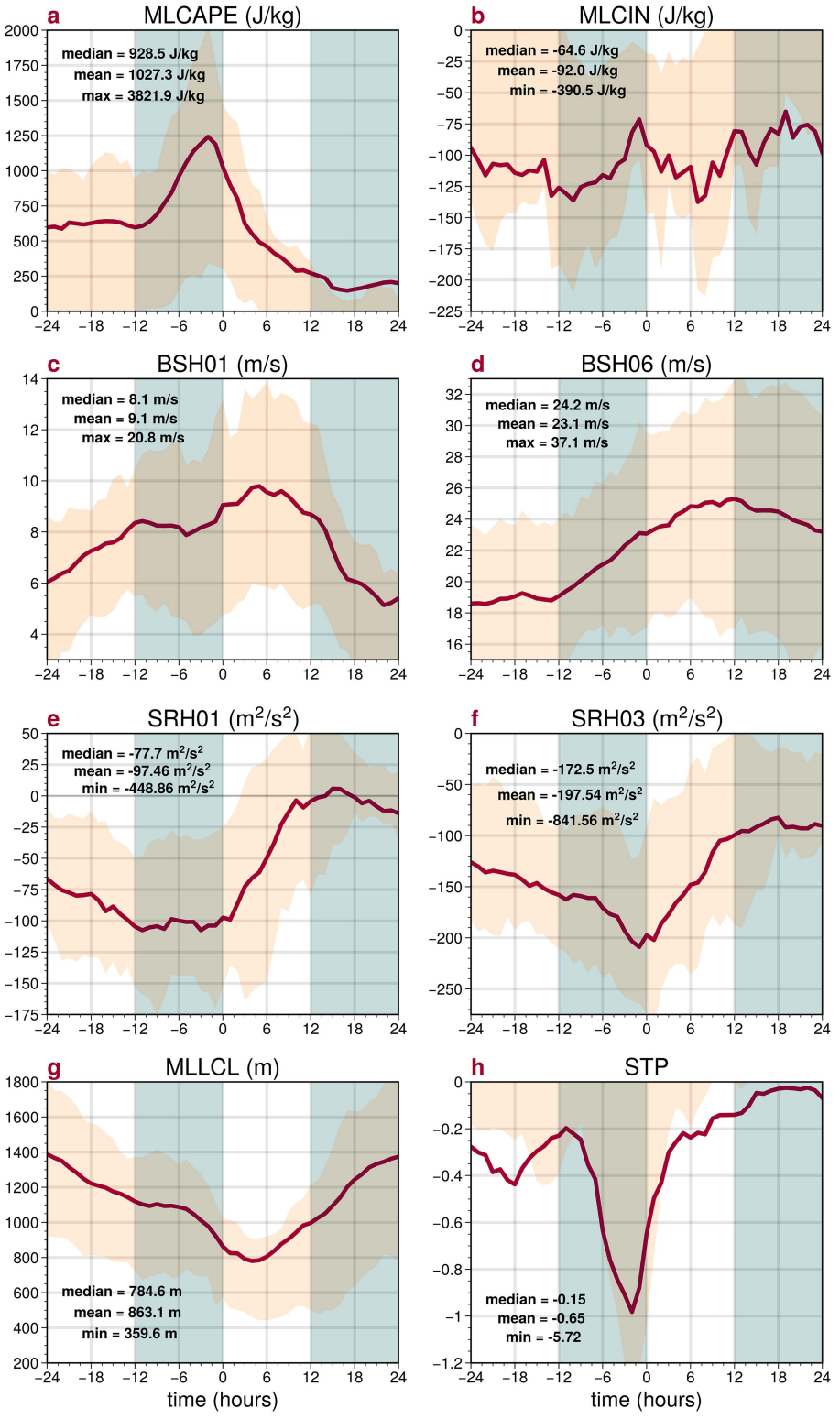

FIG. 6. Composite evolution of several convective parameters through a 48-h period centered at the time of occurrence of each event, obtained by selecting the closest proximity sounding (i.e., closest grid point) to every tornado. Light red shading indicates the spread of the interquartile range, while the dark red line shows the mean evolution. Summary statistics at hour 0 are included as text for every parameter. Vertical shading highlights 6-h spans.

The low-level environment near the storm presents an interesting evolution. Both BSH01 and SRH01 increase in magnitude 24 to 12 h before the tornado, and then stay relatively steady (about 8 to 8.5 m s^{-1} and −105 to −100 m^2 s^{-2}) up to the tornado time. No clear peak was observed for these variables. BSH01 in SESA at hour 0 (median of ~8 m s^{-1}) is significantly weaker than in the U.S. low-level environment, where it is ~15–20 m s^{-1} for F2+ tornadoes, depending on the storm mode (T12; T20), but it approaches 10 m s^{-1} for F0 events. Similar differences are observed when contrasting SRH01 (median of ~−80 m^2 s^{-2}), at best reaching nontornadic severe storms median values observed in the United States (T12). The mid- to deep-layer environment behaves differently. BSH06 shows a nearly linear increase from more than 12 h before the tornado (~19 m s^{-1}) through 6 h after (~25 m s^{-1}). SRH03 increases in magnitude at a constant rate that becomes steeper after −6 h, reaching a minimum of about −210 m^2 s^{-2} at −2 h, followed by a rapid decrease in magnitude until it stabilizes at about −90 m^2 s^{-2} past +12 h. In comparison, both BSH06 and SRH03 are as strong as for U.S. tornado environments (median ~25 m s^{-1} and >180 m^2 s^{-2} at 0 h in T12; T20). It is important to highlight the connection between the SRH03 maximum and tornado occurrence (Rasmussen and Blanchard 1998; T12; T20), as the quick increase in this parameter might reflect storms becoming tornadic when moving over a local high SRH region (Markowski et al. 1998).

Two additional shear layers (0–2 and 0–3 km), not commonly used to forecast severe storms, were also explored due to past research showing that the SALLJ is deeper than similar low-level jets in the United States (Sasaki et al. 2022; Rasmussen and Houze 2016) and the fact that the 0–3-km shear could have some forecast potential for MCS tornadoes in the United States (e.g., Gibbs 2021). Unlike BSH01 and BSH06, these shear parameters show overall larger values that are consistent with the layer size increase, and (interestingly) peak at 0 h. More analyses are needed to explore the role of 0–2- and 0–3-km shear layers in tornadogenesis over SESA, which is a subject for future research.

Evidence suggests that a low cloud-base height (estimated by the MLLCL) is important for tornadic storm environments (Brooks et al. 2003; Markowski and Richardson 2009; Thompson et al. 2012). The time evolution of the MLLCL is very similar to BSH01, with a decrease in height between −24 and −12 h, steady behavior at ~1100 m for 6–8 h, and then an absolute minimum is reached (~750 m) 4 h after the tornado. The MLLCL is about 863 m at the time of the event (median of 785 m), broadly consistent with values observed for U.S. tornado environments (T12; T20).

Finally, the STP is a composite parameter created to support operational forecasts by discriminating tornadic/nontornadic environments (Thompson et al. 2003). In our analysis, the STP demonstrates a linear increase in magnitude from about −11 until −2 h with a maximum of about −1, and then a sharp decrease (mean and median of −0.65 and −0.15 at 0 h, respectively). Of the parameters used to calculate STP, its evolution resembles that of CAPE the most. STP values below 1 in magnitude are in general not supportive of supercell tornado environments in the United States (e.g., Thompson et al. 2003; Grams et al. 2012; T20), so it may not be as useful for operational forecast of significant tornadoes in SESA given the values at the time of occurrence. However, this threshold can vary depending on the environment (e.g., Sherburn and Parker 2014; Anderson-Frey et al. 2017) and here we are compositing quite a range of environments. Moreover, the presumably small fraction of tornado reports with intensity F2+ used here, along with the inclusion of non-supercell tornadoes in the composites might also explain the reduced composite STP values at the time of occurrence. Indeed, median estimations of STP for U.S. tornadic environments using ERA5 at the time of occurrence (T20) are of ~0.4 for F2–F3 tornadoes (~1.0 for F4–F5), which is well above the 0.15 obtained for SESA. Regardless, STP peaking prior to tornado occurrence reflects that the tornadic environment in SESA is showing enhancement in some of the same key ingredients for tornadogenesis as for the United States, but the typical threshold values may need to be carefully reviewed in operational forecasting applications.

b. Mesoscale regional environment

To provide greater context to the storm evolution results, fixed-domain spatial evolution composite maps are generated. These maps give important information related to the geographic and topographic features of the region (i.e., the Andes and Sierras de Córdoba, and the Atlantic Ocean) and how they may influence the tornadic environments in SESA. Figure 7 shows the composite spatial evolution of SRH01 from −12 to +12 h with respect to the tornadic events. Enhanced negative helicity that develops along the Pampas at −12 h evolves into a maximum in SRH01, settling over southern Uruguay at 0 h and remaining relatively stationary for the next 6 h. Interestingly, the negative SRH01 peak (110–125 m^2 s^{-2}) is not located over the area with the highest concentration of tornado reports. On the other hand, a positive helicity region located to the south of the SDC emerges and grows in size and magnitude up to 75–90 m^2 s^{-2} after 0 h. Consistently, almost no tornadoes were reported over that area, although anticyclonic tornadoes under positive SRH are likely near complex terrain (e.g., Carbajal et al. 2019). Prior to tornado occurrence, the BSH01 field shows near-zero values collocated with the positive SRH01 area. The most plausible explanation for this phenomenon is simply that the signature reflects cold front passage. This idea is reinforced by what tornado-relative composite maps of SRH01 and BSH01 show: a similar SW–NE-oriented dipole structure that is more evident during and after tornado occurrence as well (not shown). Another idea to explain this positive SRH01 might be the presence of the SDC, which acts as a barrier that distorts the northerly flux coming to the mountains. During and after tornado occurrences, southerly shear is located south of the SDC, thereby reinforcing the positive SRH01 anomaly. This southerly flow might be related to the returning flow from the midlevel anomalous trough passage and subsequent lee cyclogenesis (Fig. 10), as shown by other studies (Rasmussen and Houze 2016; Piersante et al. 2021). The Andes may also play a role; their elevation and steepness may make zonal winds weak in the first 2 km, as evidenced by the composite

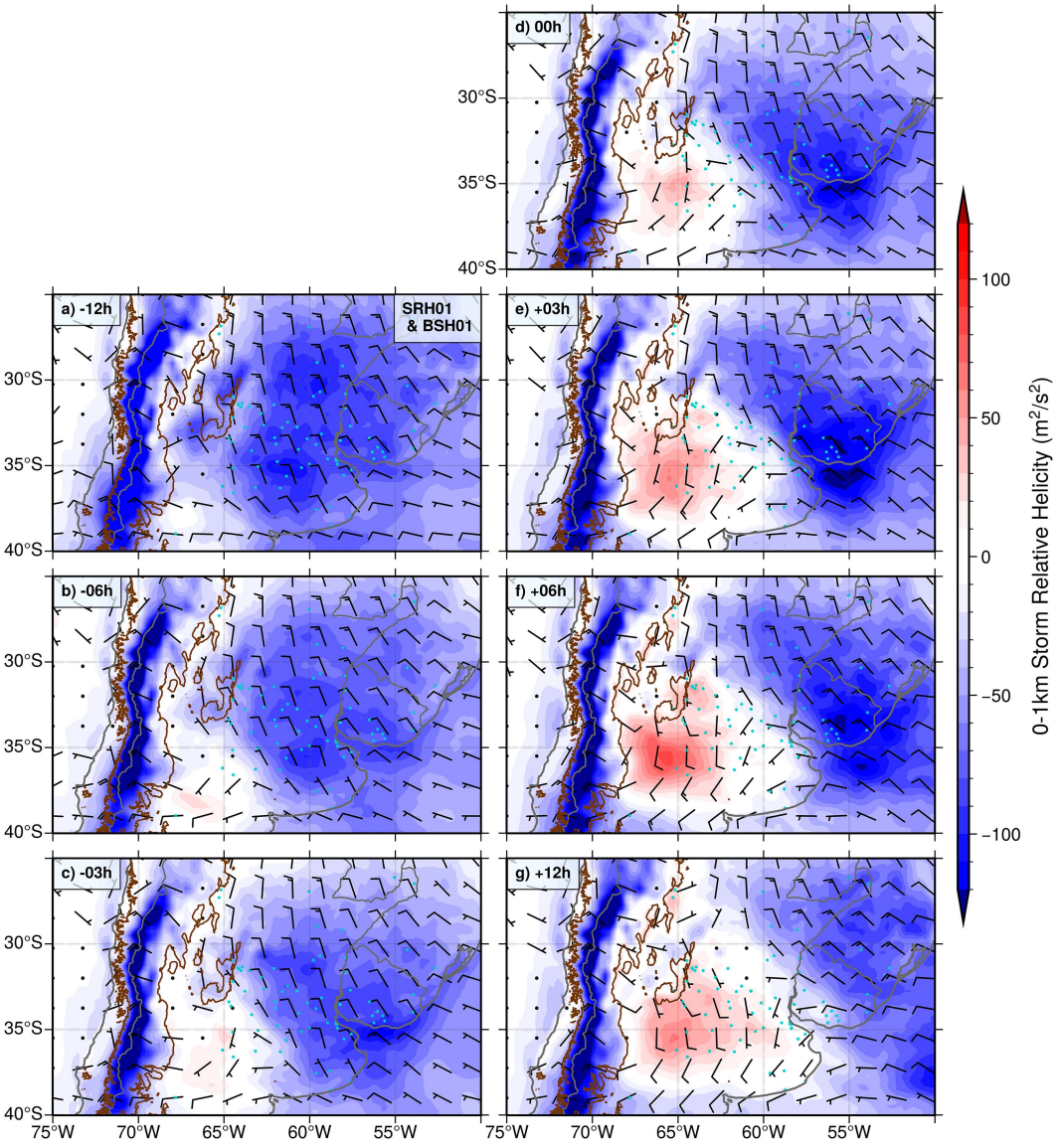

FIG. 7. Composite fields of 0–1-km storm-relative helicity (shaded) and 0–1-km bulk wind difference (wind barbs) at (a) −12, (b) −6, (c) −3, (d) 0, (e) +3, (f) +6, and (g) +12 h with respect to the tornado occurrence in SESA. Short barbs indicate 2.5 m s^{-1} while long barbs indicate 5 m s^{-1}. The 800-m AGL elevation is indicated with brown contours to help the reader better visualize the main topographic features. Turquoise dots show the location of the tornadoes used in this study.

hodograph (Fig. 5). Further analyses are needed to investigate these hypotheses that are beyond the scope of the current study.

Figure 8 shows the composite spatial evolution of STP. This parameter increases in magnitude starting at −12 h, reaches its maximum extent a few hours before and at the time of tornado occurrence, and then diminishes by +12 h. The position of the maximum STP (shading below −0.4) matches well with the region where most of the tornadoes occur. The maximum magnitude of composite STP from Fig. 8 approaches 1 (in apparent agreement with the Fig. 6h magnitude maximum), but some individual cases can present higher STP (see the STP spread in Fig. 6h). Indeed, there are instances where STP can reach values significantly lower than −1, especially east and southeast of the SDC (not shown). However, since our composites are derived from tornadoes occurring at distinct locations, reduced values are expected at any given spatial location.

To further explore the spatial signature of STP before and after tornadogenesis in SESA, tornado-relative composite maps of STP are computed. Figure 9 presents these maps for a ~22° latitude × ~15° longitude (89 × 61 grid points) domain, with the tornadic storm report locations at the center of the map. It is evident from the temporal evolution of STP that the maximum values are reached in the −3- to 0-h timeframe,

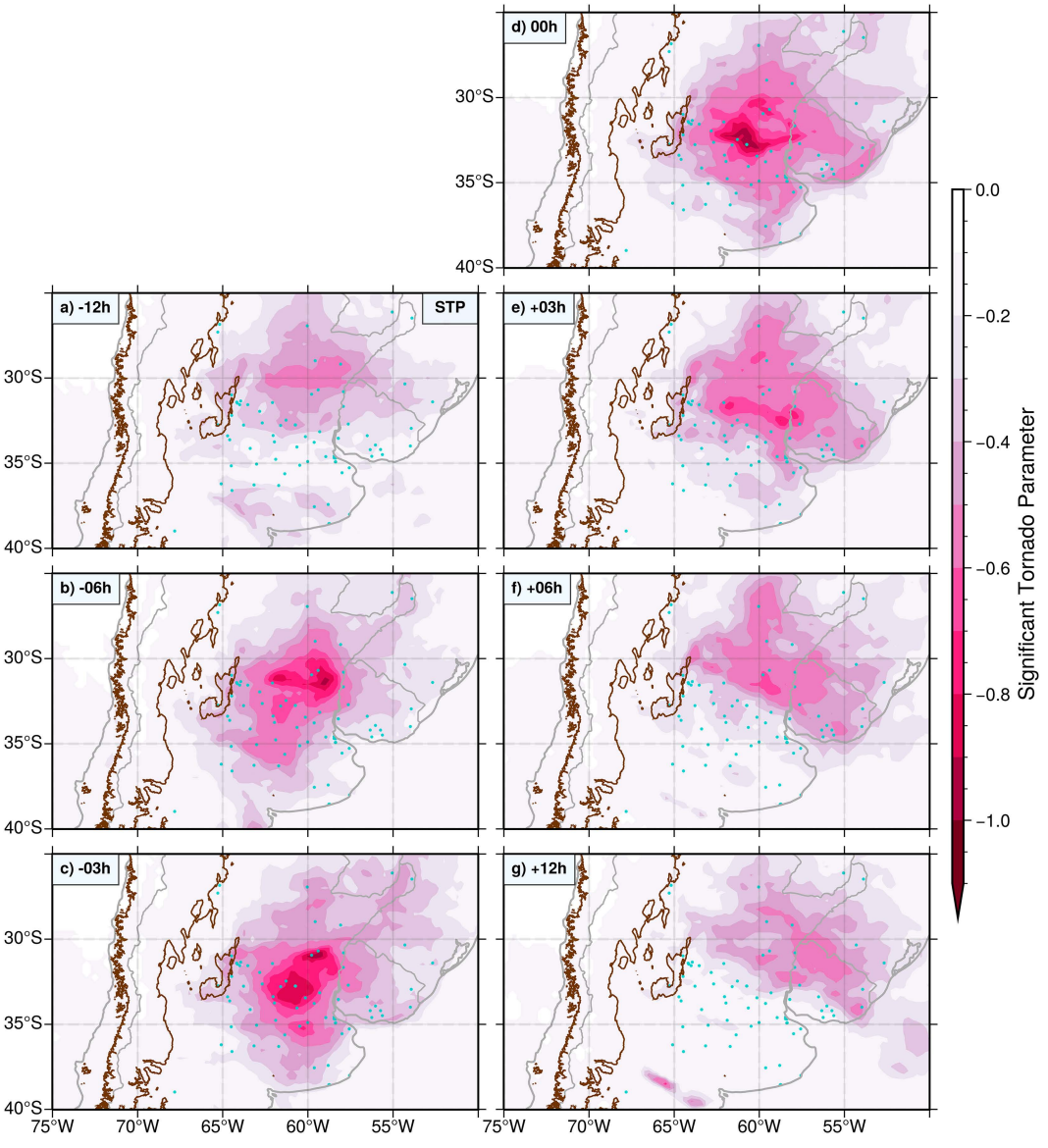

FIG. 8. Composite fields of significant tornado parameter (shaded) at (a) −12, (b) −6, (c) −3, (d) 0, (e) +3, (f) +6, and (g) +12 h with respect to the tornado occurrence in SESA. The 800-m AGL elevation is indicated with brown contours to help the reader better visualize the main topographic features. Turquoise dots show the location of the tornadoes used in this study.

when STP is, on average, larger than 1 in magnitude and about 0.25°–0.75° north of the tornado location. In other words, this indicates that tornadoes are taking place just south-southwest of a peak in STP, which could further support the idea of storms becoming tornadic when entering a high STP region (which is also a high SRH region, not shown) (Markowski et al. 1998). More analysis is needed to elucidate this connection. The fact that high STP values are seen predominantly equatorward from where a tornado eventually occurs (and near-zero values poleward of it) gives an idea of the placement of the inflow of the storms. Figure 9 also shows composites of MLCAPE peaking equatorward of the tornado's position at −3 and 0 h (>1500 J kg^{-1}), but with the most unstable region located north of the STP maximum. At the tornado location, MLCAPE presents its largest spatial gradient. Parker (2014) used observational data to show that a peak in STP is also located just equatorward from supercell tornadoes observed in the United States and that this STP feature is significantly weaker and less organized when compared to nontornadic supercells. Other studies addressing various tornado environments have also found STP peaking equatorward of tornadogenesis regions as a recurrent feature (Sherburn et al. 2016; Anderson-Frey et al. 2017). This finding could provide additional insight in anticipating areas for tornadogenesis over SESA.

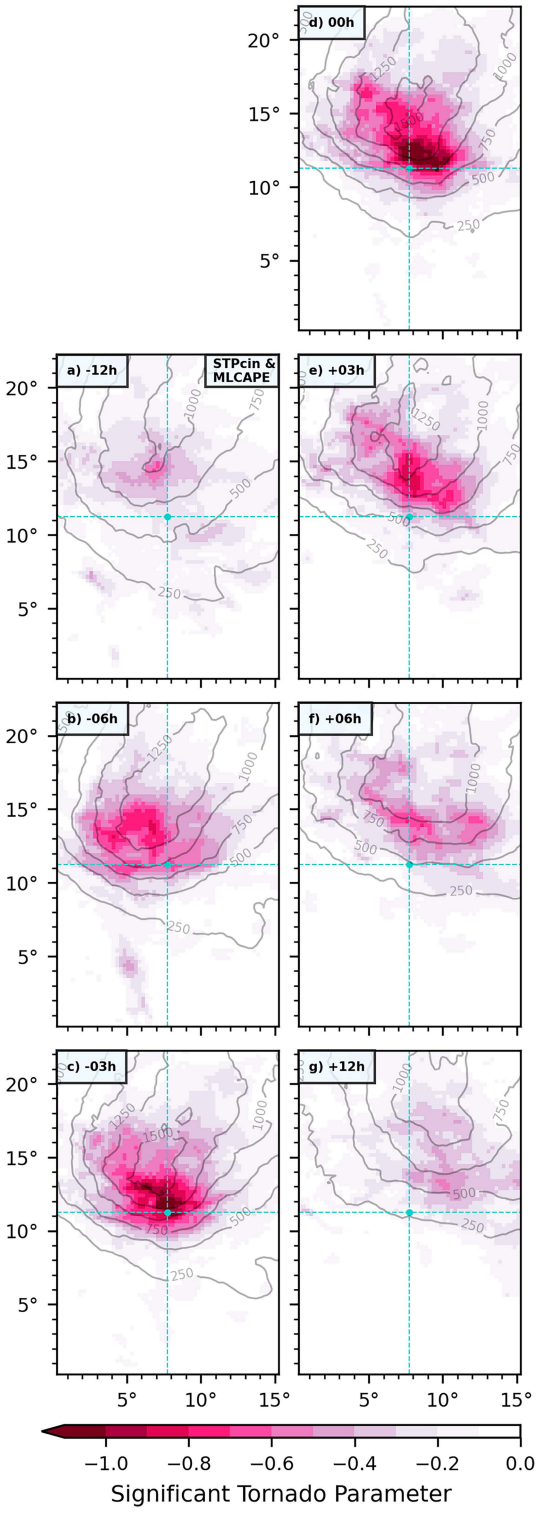

FIG. 9. Tornado-relative composite maps of significant tornado parameter (shaded) and mixed-layer CAPE (gray contours, every 250 J kg^{-1}) at (a) −12, (b) −6, (c) −3, (d) 0, (e) +3, (f) +6, and (g) +12 h with respect to the tornado occurrence in SESA. Maps correspond to a domain of 89 × 61 grid points (~22° latitude × ~15° longitude) centered at the location of the tornadic storms (cyan circle).

c. *Tornadic storm comparison between SESA and the U.S. Great Plains*

It is believed that tornadoes are more frequent in the U.S. Great Plains than in SESA plains, even though population density in countries like Argentina is relatively lower compared to the United States. Despite their geographical similarities, it is important to note some differences that may shed light in frequency disparities. The Andes are taller and narrower than the Rockies in the subtropics, leading to enhanced CAPE and CIN in SESA that often require the additional lifting motion provided by secondary topographic features such as the SDC in Argentina (Rasmussen and Houze 2016). This can affect the initiation and evolution of deep and severe convection downstream, as has been evidenced by recent studies (Rasmussen and Houze 2016; Nesbitt et al. 2021; Rocque and Rasmussen 2022). In addition, the U.S. land extension, including the Great Plains and eastern United States, is much larger than the Pampas region over Argentina, where the distance between the Andes and the Atlantic coast becomes shorter poleward (Fig. 1). This reduced land extension in southern Argentina can prevent the formation of an appropriate severe environment further south. Indeed, tornadoes are very frequent up to the northernmost state in the central United States (46°–49°N), while beyond 38°–40°S in Argentina these seem to be exceptional (e.g., Fig. 1; Schwarzkopf 1988).

Other reasons may be related to the convective environment. Recent results from Schumacher et al. (2021) depicted weak 0–1-km winds being relatively frequent during convective days in the RELAMPAGO field campaign that occurred in central Argentina, with a median of 4.9 m s^{-1} for BSH01 across all the soundings (R. Schumacher 2022, personal communication). These observations suggest that the typical 0–1-km wind shear is hardly supportive of tornadic storms in SESA in the RELAMPAGO study region. Actually, no tornadoes were officially measured or sighted during the campaign (though our own tornado database includes two events that happened during the RELAMPAGO deployment, but away from the operation sites). Results from Lopes (2020), who analyzed 40 tornado events in southern Brazil using the Climate Forecast System Reanalysis, presented higher values for low-level dynamic parameters (median for BSH01 ~ 12 m s^{-1}, SRH01 ~ −140 m^2 s^{-2}) and surface-based CAPE (~1400 J kg^{-1}). This difference with our results may suggest spatial variability of the tornadic environment within SESA as our study considered only a few reports from southern Brazil. For example, isolating tornadoes closer to the mountains in Fig. 4b mostly indicates BSH01 below 5 m s^{-1}, with only 7 out of 32 cases having values over 10 m s^{-1}, which is also consistent with the weak low-level shear environment in the RELAMPAGO domain (Schumacher et al. 2021). Therefore, having weak low-level winds might imply that tornadoes need to overcome a less favorable environment to be produced, which can occur less frequently. However, the stronger BSH01 environment observed east of La Plata Basin in Lopes (2020) might also be due to 30% of the tornadoes occurring in wintertime having a stronger low-level jet (Montini et al. 2019), related to more frequent synoptic forcing (Nascimento et al. 2016; Marengo et al. 2004). The weak low-level flow for SESA tornadoes could also be

associated with weak tornadoes. Tornadoes generated in the United States have different BSH01 values when split into significant (F2+, ~16 m s^{-1}) and nonsignificant (F0–F1, ~10 m s^{-1}) tornadoes (T20). Our study did not have enough intensity information reported to connect these results to tornado intensity, however. Another factor that could explain differences observed in the low-level flow is the distinct moisture sources in North and South America and associated surface roughness. Li et al. (2023, manuscript submitted to *Nat. Portfolio*) conducted modeling experiments that replaced and smoothed the land equatorward of SESA with an ocean-like surface (similar to North America), which enhanced the low-level winds and, subsequently, the potential for tornadogenesis. Opposite results were observed for the United States when the Gulf of Mexico was replaced by forest-like land with increased surface roughness.

The apparently less favorable environment for tornadogenesis in SESA is also evidenced in the STP composites (Figs. 6h and 8), especially when contrasting median values at the time of occurrence. Given the geographical similarities with severe weather environments in the United States, there is value in comparing the STP for SESA with similar calculations in the United States. Indeed, tornado-relative spatial composites of STP (Fig. 9) illustrated similar equatorward placement of the peak in STP centered on tornadic storm report locations. Nevertheless, potential differences in the storm modes between both regions, observed a priori in Fig. 3 and other studies (Rasmussen and Houze 2011, 2016; Rasmussen et al. 2014; Mulholland et al. 2018), may explain the difficulties in using STP for forecasting tornadoes in SESA, as this index was computed based on supercell tornado environments. Similarly, storm-relative helicity computations could also be affected by the tornado storm mode, as they rely on estimated storm motion from supercells (Bunkers et al. 2014). More comprehensive analyses would need to be done (including detailed field measurements) to determine if most tornadoes occur in MCSs as opposed to supercells.

5. Larger-scale environments modulating tornadic storms

In this section, the synoptic- and planetary-scale environments supporting the development of tornadic storms in SESA are examined to provide context to the mesoscale analyses presented in the previous section. Remote sources of predictability in the tropics will be also explored.

a. Synoptic scale

Figure 10 presents the composite 850- and 500-hPa geopotential height anomaly fields based on the 74 tornado reports collected over SESA, between 2 days before and 2 days after the events. Two days before a tornado, negative 500-hPa geopotential height anomalies related to a trough located south of 30°S over the South Pacific impinge on the southern tip of South America (Fig. 10a). This trough then slowly moves to the northeast, placing its center over Patagonia while lee cyclogenesis emerges in central and northern Argentina by day 0 (Figs. 10b,c). This slow-moving system (~5–10 m s^{-1}, according to our estimations of mean displacement per day) may contribute to the abundance and severity of the storms as the persistence of the forcing maintains the unstable environment for a longer time, consistent with, for example, tornado outbreaks in the United States (e.g., Hamill et al. 2005; Mercer et al. 2012; Knupp et al. 2014). In fact, 15%–20% of our tornado database considers events where two or more tornadoes occurred in the same day (Veloso-Aguila 2023), but these repeat events were considered as only 1 day for the composite analyses. After day 0, the 500-hPa trough starts to move faster, crossing the Andes completely with its center located over the Atlantic south of 40°S, while the intensity of the anomalies decays by 20 m. The evolution of cyclonic anomalies at the 850-hPa level is similar to that at 500 hPa during the previous 2 days, except that lee cyclogenesis occurs along the Andes foothills up to about 20°S when tornadoes occur. The cyclogenesis in the lee of the Andes is maximized over the central Pampas and the northern Andes foothills in Argentina. In the period after the tornado (Figs. 10d,e), the negative 850-hPa anomalies start to diminish along the eastern edge of the Andes, while the low pressure system at 850 hPa moves to the southeast at a faster rate than its counterpart at 500 hPa. The positive anomalies located over the Atlantic around 40°S and to the east of the trough are likely also important to the generation of the severe weather environment. When coupled with the trough, the ridge may aid the generation of northerly flow anomalies, especially at low levels, which produces enhanced moisture transport associated with the SALLJ (Vera et al. 2006; Rasmussen et al. 2016; Sasaki et al. 2022) impinging upon the tornado region.

To support this hypothesis, Fig. 11 shows anomalies of 850-hPa specific humidity and winds. The transport of water vapor from the Amazon to the Pampas region maximizes around the time the tornadoes take place. While the humidity anomalies maximize over the central Pampas (Figs. 11c,d), the maximum humidity transport anomalies (for the entire air column) occur in the Andes foothills between southern Bolivia and northwestern Argentina (not shown), where a strong 850-hPa humidity gradient is present and the SALLJ (Figs. 11c,d) is enhanced by the anticyclonic anomalies over the Atlantic and the low pressure system around 30°S (Fig. 10). The lee cyclogenesis in this region creates a pressure gradient that enhances the winds to the south, thus maximizing the humidity advection between 20° and 30°S (Rasmussen and Houze 2016). This humidity transport is a key component in the tornadogenesis over SESA, which helps boosting the instability there (i.e., CAPE enhancement, Fig. 6a). However, elevated mixed-layers, which are relevant features for severe thunderstorms east of major mountain ranges, (e.g., Ribeiro and Bosart 2018), could also contribute to the CAPE generation before tornadogenesis, presenting avenues for future investigation. The moisture advection also sets the stage to produce severe storms when superposed with high vertical wind shear (induced by the synoptic forcing that enhances the meridional low-level jet and the westerlies at midlevels; Figs. 10–12) (Piersante et al. 2021) and lifting mechanisms (e.g., orographic lifting caused by small topographic features). However, for tornado events that occur closer to the Atlantic Ocean, there may be a role for low-level moisture advection from oceanic sources as well. The synoptic composite results are notably like those presented by Rasmussen and Houze (2016) connected with convective modes associated

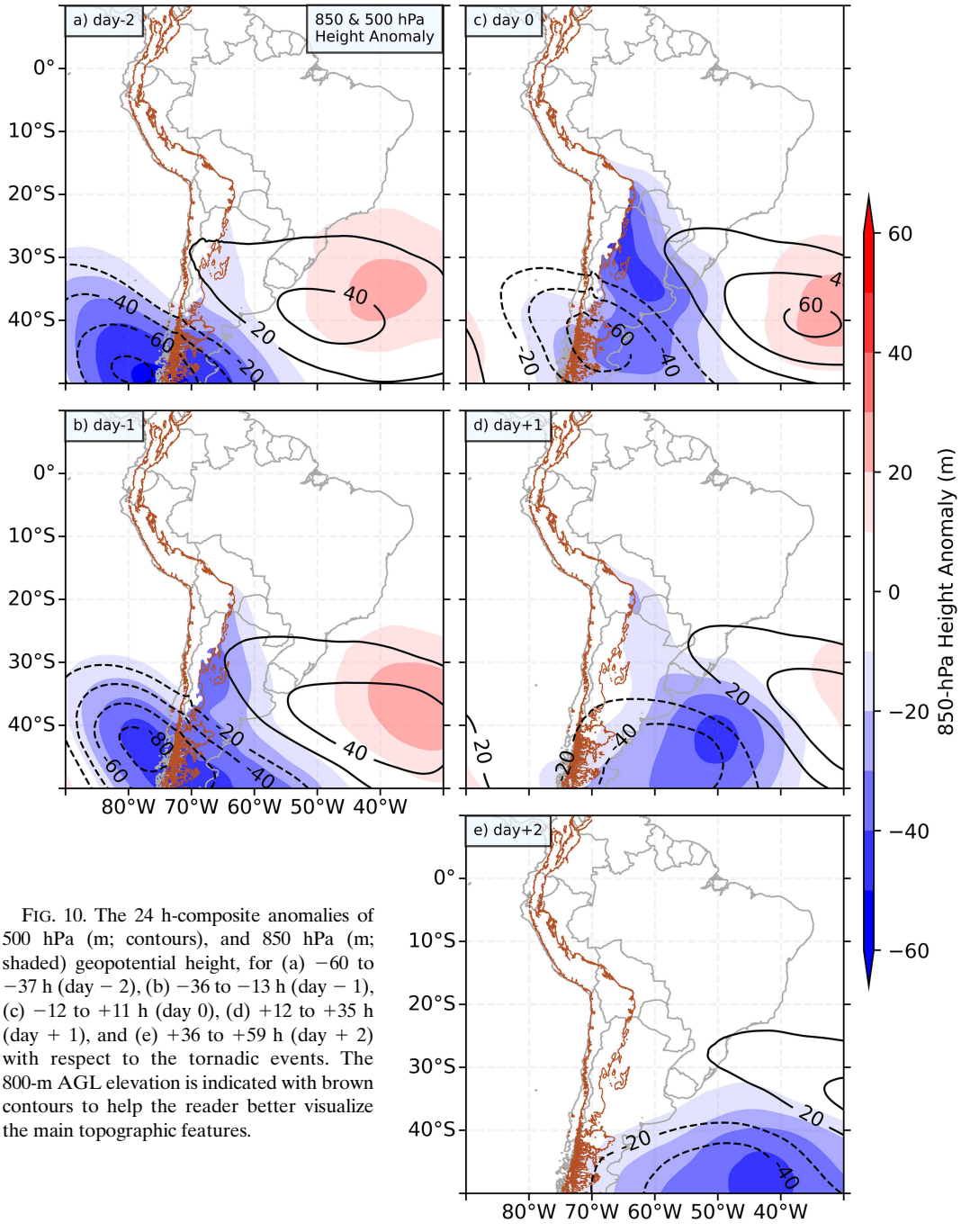

FIG. 10. The 24 h-composite anomalies of 500 hPa (m; contours), and 850 hPa (m; shaded) geopotential height, for (a) −60 to −37 h (day − 2), (b) −36 to −13 h (day − 1), (c) −12 to +11 h (day 0), (d) +12 to +35 h (day + 1), and (e) +36 to +59 h (day + 2) with respect to the tornadic events. The 800-m AGL elevation is indicated with brown contours to help the reader better visualize the main topographic features.

with MCSs, providing support for the importance of large-scale forcing in severe weather environments in SESA in general. When partitioning the synoptic evolution composites by seasons, although modest variations in location and intensity, qualitatively similar synoptic features modulating the convective environment are seen (not shown). These results stand in contrast to Piersante et al. (2021) that showed strong synoptic forcing in austral spring (SON) and much weaker forcing in austral summer (DJF). As such, tornadic events in SESA appear to be strongly forced at the synoptic scale regardless of the season.

b. *Planetary scale and teleconnections*

Several previous studies have examined how synoptic-scale modulate convective storms and severe weather production in SESA (Rasmussen and Houze 2011, 2016; Rasmussen et al. 2014; Piersante et al. 2021; Lopes 2020). However, a connection to planetary-scale patterns connected to tornado events

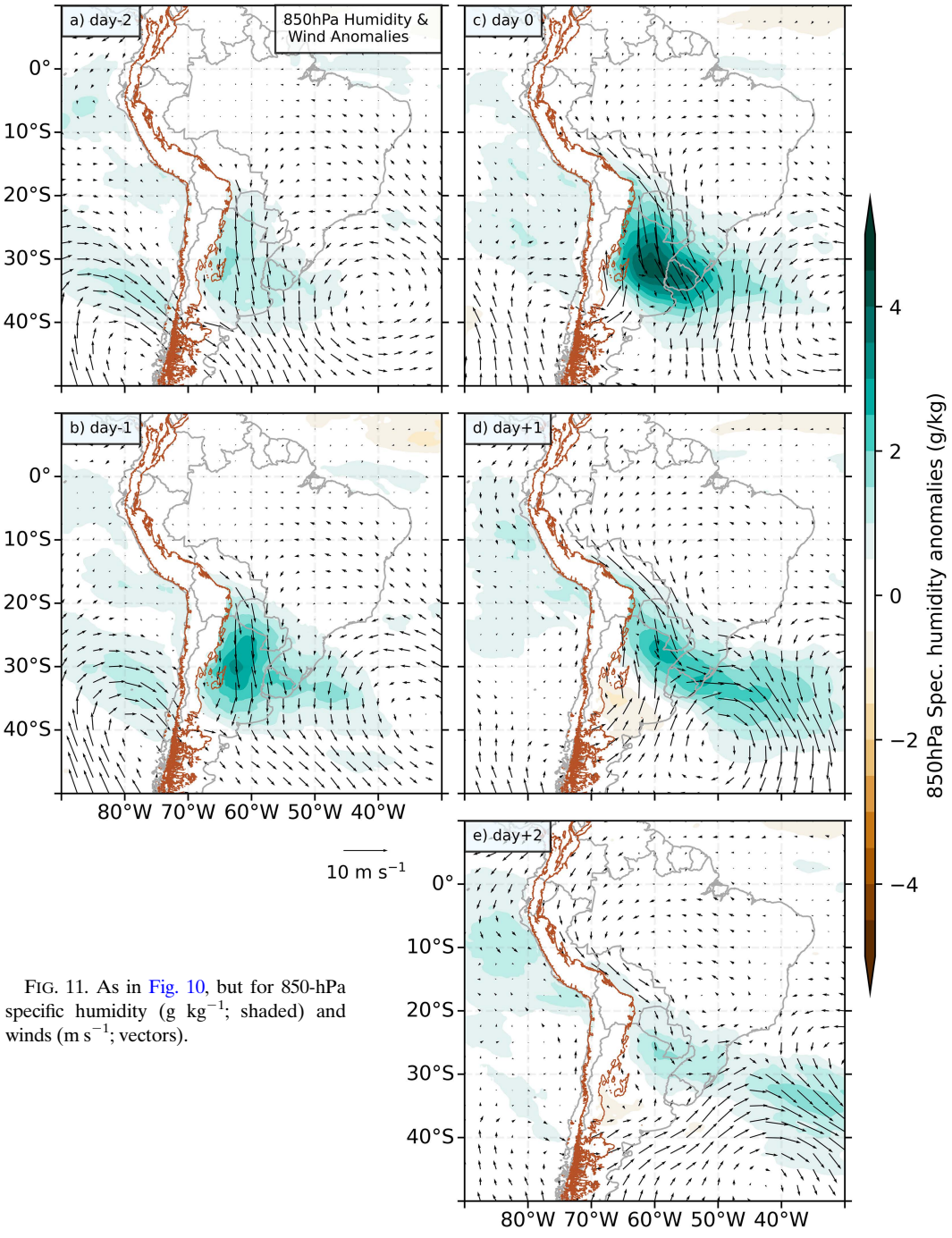

FIG. 11. As in Fig. 10, but for 850-hPa specific humidity (g kg^{-1}; shaded) and winds (m s^{-1}; vectors).

in SESA has not previously been examined in detail. To address this gap, we examine how global teleconnection patterns influence tornadic storms in SESA. The 250-hPa geopotential height and zonal wind anomalies (Fig. 12) show a well-defined wave train pattern connecting South America and the tropical west Pacific a few days before a tornado occurs. The pattern resembles the PSA pattern found in previous studies (Mo and Higgins 1998; Mo and Paegle 2001), which can be modulated by remote heating with the MJO and other phenomena. The trough–ridge–trough pattern can be traced up to 7–9 days prior to a tornado event in SESA and diminished afterward (not shown). The portion of the wave train located over South America resembles the pattern analyzed in the 500- and 850-hPa fields (Fig. 10) and in prior research (Rasmussen and Houze 2011, 2016; Piersante et al. 2021), where an anomalous trough located over southern Chile is about to cross the Andes, flanked by an anomalous downstream ridge. Another interesting aspect is that the ridge located over the Southern

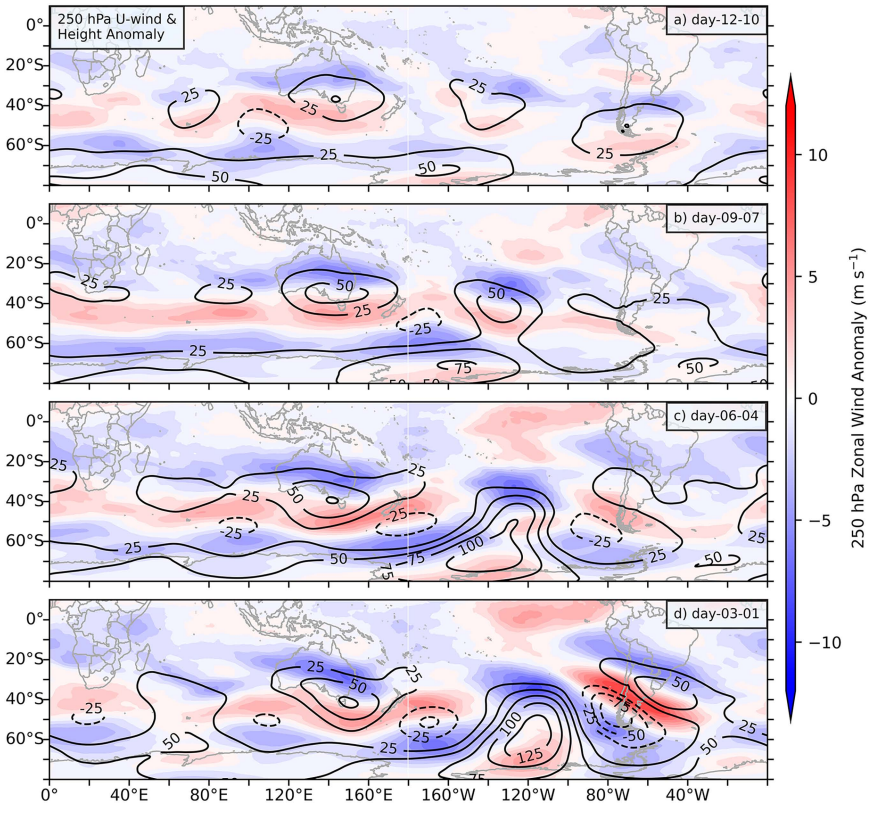

FIG. 12. Triad composite anomalies of the 250-hPa geopotential height (m; contours) and zonal wind (m s^{-1}; shaded) prior to the development of tornadoes in SESA, (a) 10–12, (b) 7–9, (c) 4–6, and (d) 1–3 days before the events.

Ocean around 140°–120°W (Figs. 12c,d) intensifies a few days before the tornado day, possibly supporting downstream amplification of the wave pattern over South America and its northeastward displacement. A detailed examination of individual cases could confirm this hypothesis, including a possible role for wave breaking, which is left for future work. Thus, it appears that the strong synoptic forcing accompanying severe thunderstorms in SESA is connected to large-scale circulations having a remote origin.

To get insights into the initiation mechanism of the stationary Rossby wave train pattern influencing severe weather in South America, composites of outgoing longwave radiation (OLR) anomalies are computed (Fig. 13). A negative OLR signal, indicating cold cloud tops and deep convection, is prominent on the northwestern Australian coast 7 to 9 days before the tornadic storms develop in SESA. This signal strengthens by days −4 to −6, and then begins to diminish. Negative OLR anomalies are indicative of enhanced convection occurring over the area, which may provide a Rossby wave source that produces the wave train signal seen in the composite 250-hPa field. Composites of the PSA modes conducted by Mo and Paegle (2001) show a similar wave train pattern connected to convection in the Maritime Continent that resembles that of Fig. 12d. The fact that the OLR anomalies are stronger for the −4 to −6 triad in Fig. 13 versus a stronger Rossby wave pattern on the −1 to −3 triad in Fig. 12 gives some support to the idea that anomalous convection over northwestern Australia triggers a wave train that arrives in South America a few days later.

Previous studies have shown that disturbances like the MJO can produce teleconnection patterns such as this (e.g., Grimm 2019; Sena et al. 2022). An analysis of the distribution of the MJO phases from 15 to 0 days prior to the development of every tornado event is performed, including a breakdown by season (Fig. 14). The histograms show that when all months are considered, tornadoes are most frequent when the MJO is active in phase 3 (20%). Phases 2 and 4 are the second most frequent (near 15% each), but their values are not significantly different from random chance across all phases. A breakdown of the distribution into shorter periods (e.g., triads, like Figs. 12 and 13) showed no significant differences in the predominant phases. Composite MJO events tend to have enhanced convection to the northwest of Australia in association with these phases (Wheeler and Hendon 2004), although generally further away from the continent than shown in our Fig. 13 OLR composites. This mismatch is probably caused by the poor representation by the RMM index of the MJO convection as its computation is dominated by the wind components rather than OLR [see Straub (2013), and Liu et al. (2016) for further details]. Phase 5 also shows significant

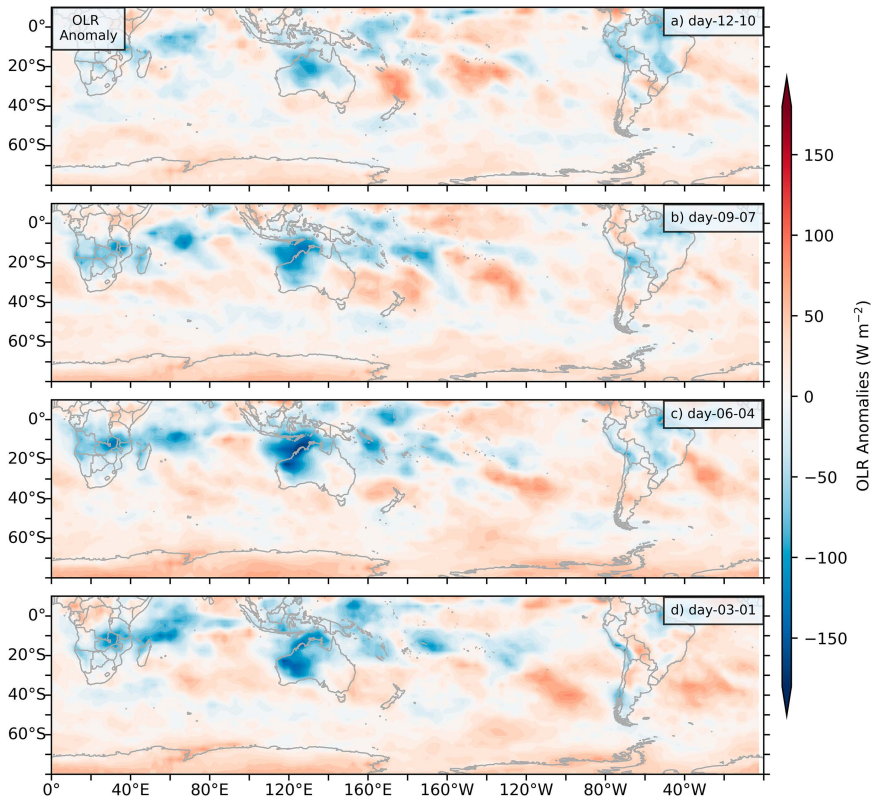

FIG. 13. As in Fig. 12, but for outgoing longwave radiation anomalies (W m^{-2}; shaded).

suppression of tornadic storms. In terms of the seasonal distribution, both summer and autumn tornadoes are dominated by MJO phase 3 during the previous two weeks (~25%), though the MJO phases that exhibit a significant suppression of tornadic activity are not consistent (phases 1 and 8 for DJF versus phases 1 and 5 for MAM, between 5% and 8%). The spring season presents a distinct distribution, however. The active MJO phases associated with most frequent tornadoes (over 17%) are phases 1, 2, and 4, with the latter showing the highest frequency (~21%). On the contrary, phases 5, 6, and 7 show significant tornado suppression (below 8%), with phase 6 being present in only 3% of the events. In this regard, the impact of the MJO on tornado formation seems to vary more smoothly during SON, versus DJF and MAM which are noisier.

6. Conclusions

The environment supportive of tornadic storms in southeast South America (SESA) is analyzed, focusing on the mesoscale, synoptic, and planetary-scale patterns that contribute to their development. Tropical teleconnections that contribute to these large-scale patterns were assessed. This is the first time that the supporting environment for tornadoes in SESA has been studied on a multiscale basis, based on a new self-constructed database of reports from the last 30 years and using novel reanalysis data with high spatial and temporal resolution. Results highlight important similarities in the convective environment that sustains tornadoes in the United States and SESA, though key dissimilarities in some parameters were found.

Consistent with a convective season that is active from spring through fall (Zipser et al. 2006; Rasmussen and Houze 2011), the tornado database used here shows that tornadoes in SESA are relatively common in all seasons except winter (Fig. 2a). Tornadoes mostly form in late afternoon, although they sometimes occur in the evening and during the night (Fig. 2b). The spatial distribution of reports was found to be like the distribution of events collected over earlier periods of the twentieth century for Argentina (Schwarzkopf 1988), with most the reports over the plains, and only a few near the Andes foothills (Fig. 1). Lack of reports south of the Sierras de Córdoba (Fig. 1) is consistent with unfavorable conditions for tornado formation observed there (Figs. 7 and 8).

ISCCP data were used to show that tornadoes in SESA are embedded in a wide variety of storm sizes, ranging from discrete storms to large MCSs (Fig. 3). Tornadoes appear to be more regularly embedded in isolated thunderstorms or small MCSs rather than large convective systems. Nocturnal tornadoes are associated with 20% larger cloud shield systems compared to daytime events.

Several dynamic and thermodynamic parameters known to influence tornadic environments were composited across all the tornadoes reported. Proximity environment evolution

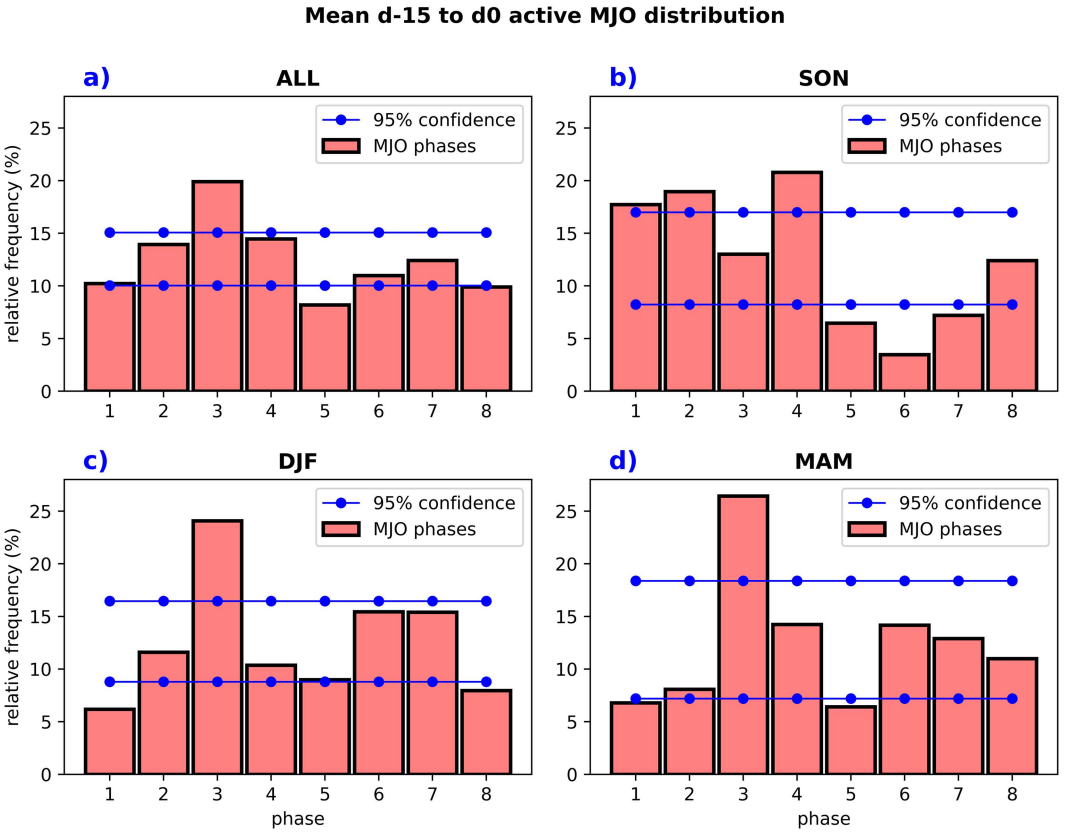

FIG. 14. Histogram of the MJO active phase distribution for the 16-day period prior to the tornadic events, considering (a) all events, (b) SON, (c) DJF, and (d) MAM events only. The 95% confidence interval (blue line) is computed by applying a bootstrap test with 10 000 realizations.

before and during tornadoes showed that strong instability, deep-layer vertical shear, and storm-relative helicity need to be built, while convective inhibition and lifting condensation level need to be reduced, prior to or during the development of tornadic storms in SESA (Fig. 6). At the time of tornado occurrence, high-CAPE, high-BSH06, and low-LCL were generally preferred while no clear preference was observed for BSH01, though particularly low values were observed for most of the events close to the high terrain (Fig. 4). Also, a curved hodograph with anticyclonic rotation was observed, presenting strong low-level directional shear but weak speed shear (Fig. 5).

The SESA tornadic environments analyzed in this study are compared with other studies focused on U.S. Great Plains tornadoes. In SESA, parameters such as MLCAPE, BSH06, and MLLCL presented values broadly supportive of tornadic storms, according to typical U.S. values. However, weak low-level dynamic environments (BSH01 and SRH01) and moderate convection inhibition (MLCIN) found for SESA tornadoes versus those in the United States would make their formation more difficult in the United States. This is echoed by the moderate STP values reported (Figs. 6h and 8), although an STP maximum located equatorward of the tornado locations (Fig. 9) could help determine potential areas for tornadogenesis. Thus, more research is required in determining STP's effectiveness in predicting tornadoes of all intensities in SESA. Geographical disparities, in particular the taller mountain range east of SESA relative to the Rockies and U.S. Great Plains and their impact on the generation of low-level flows and associated moisture advection, could explain some of the observed differences in frequency and environments supporting tornadic storms in the United States versus SESA. Thus, these differences should be more carefully analyzed in future work, likely in numerical modeling simulations, to understand how contrasts in topography, moisture source, wind shear generation throughout the troposphere, and environmental parameters influence the nature and evolution of tornadic storms in both continents (e.g., Li et al. 2023, manuscript submitted to *Nat. Portfolio*).

The mesoscale environments associated with tornadic storms are supported by strong synoptic forcing in both austral spring and summer that initiates cyclogenesis in the lee of the Andes (Fig. 10) and enhances the upper-level zonal winds (Fig. 12e), resulting in an enhanced SALLJ yielding sufficient moisture to aid in destabilizing the atmosphere (Fig. 11) and strong deep-layer shear supporting organized storms in the region. This forcing also provides lifting mechanisms that along with terrain features, initiate the storms that subsequently become tornadic. The anomalous trough required to set the stage for tornadic storms appears to displace slowly while crossing the Andes, so the persistence of the forcing may be a relevant factor for tornado formation in SESA.

Zooming out to hemispheric scales suggests that convection near the northwestern coast of Australia may influence SESA tornado occurrence via teleconnection patterns (i.e., Rossby waves) that influence the synoptic-scale environment over SESA. The teleconnection pattern resembles the Pacific South American pattern, found in previous studies (Mo and Higgins 1998; Mo and Paegle 2001). MJO analysis further supports the relationship of tornadoes in SESA with tropical sources, suggesting the preferred presence of phase 3 in the RMM index during the two weeks prior to a tornado event, although isolating the season of SON shows a broad enhancement of tornado activity across MJO phases 1 through 4. These results may be useful from a predictability standpoint and suggest there could be skill in identifying synoptic and mesoscale configurations that may lead to severe weather hazards—including tornadoes—over SESA up to a week or two in advance. This is the first study that connects tornadic storms in SESA to large-scale patterns induced by remote tropical sources in a climatological sense.

The multiscale approach employed here illustrates the relevance of atmospheric processes occurring at different spatial and temporal scales in the occurrence of tornadoes (Tochimoto 2022). Improving observing systems and encouraging routine collection of severe weather reports in South America are urged, as future studies using denser observational data and reports would give new and improved insights into the convective environments that support tornadoes in SESA, including validation of results from this investigation—mostly based on reanalysis data. Exploration of new sources of predictability from tropical teleconnections and elsewhere can also be extremely useful for providing early weather outlooks to emergency management agencies to prepare the population for severe weather threats, especially in highly vulnerable communities across the continent. Last, assessing future changes in the convective environment due to climate change requires comprehension of current severe weather signatures in the region, which has urgency given the increasing frequency of extreme weather across the planet.

Acknowledgments. This research was sponsored by National Science Foundation Grants AGS-1661657, AGS- 1841754, AGS-2146709, and Department of Energy Grant DE-SC0022056. Daniel Veloso-Aguila is also supported by the Equal Opportunity Fulbright-ANID Scholarship from the country of Chile. The authors thank three anonymous reviewers for their helpful reviews that have improved the manuscript. Thanks to all who contribute to the reporting of severe weather events around the world.

Data availability statement. The self-constructed tornado report database used in this study is available in Veloso-Aguila (2023). ERA5 data at single, pressure, and model level were obtained from the European Centre for Medium-Range Weather Forecasts (ECMWF), Copernicus Climate Change Service (C3S) using the Climate Data Store Application Program Interface (CDS API, https://cds.climate.copernicus.eu). The ISCCP H-Series Cloud Properties Climate Data Record dataset from the NOAA/National Centers for Environmental Information (NCEI) can be accessed at https://www.ncei.noaa.gov. NOAA interpolated outgoing longwave radiation (OLR) data are provided by the NOAA/Physical Sciences Laboratory from their website at https://psl.noaa.gov. The Real-time Multivariate MJO (RMM) index from Wheeler and Hendon (2004) was obtained from the Bureau of Meteorology, Australia (http://www.bom.gov.au/climate/mjo/graphics/rmm.74toRealtime.txt).

REFERENCES

Alvarez, M. S., C. S. Vera, G. N. Kiladis, and B. Liebmann, 2016: Influence of the Madden–Julian Oscillation on precipitation and surface air temperature in South America. *Climate Dyn.*, **46**, 245–262, https://doi.org/10.1007/s00382-015-2581-6.

Anderson, C. J., C. K. Wikle, Q. Zhou, and J. A. Royle, 2007: Population influences on tornado reports in the United States. *Wea. Forecasting*, **22**, 571–579, https://doi.org/10.1175/WAF997.1.

Anderson-Frey, A. K., Y. P. Richardson, A. R. Dean, R. L. Thompson, and B. T. Smith, 2016: Investigation of near-storm environments for tornado events and warnings. *Wea. Forecasting*, **31**, 1771–1790, https://doi.org/10.1175/WAF-D-16-0046.1.

——, ——, ——, ——, and ——, 2017: Self-organizing maps for the investigation of tornadic near-storm environments. *Wea. Forecasting*, **32**, 1467–1475, https://doi.org/10.1175/WAF-D-17-0034.1.

Baggett, C. F., K. M. Nardi, S. J. Childs, S. N. Zito, E. A. Barnes, and E. D. Maloney, 2018: Skillful subseasonal forecasts of weekly tornado and hail activity using the Madden-Julian Oscillation. *J. Geophys. Res. Atmos.*, **123**, 12 661–12 675, https://doi.org/10.1029/2018JD029059.

Banacos, P. C., and M. L. Ekster, 2010: The association of the elevated mixed layer with significant severe weather events in the northeastern United States. *Wea. Forecasting*, **25**, 1082–1102, https://doi.org/10.1175/2010WAF2222363.1.

Barrett, B. S., J. C. Marin, and M. Jacques-Coper, 2020: A multiscale analysis of the tornadoes of 30–31 May 2019 in south-central Chile. *Atmos. Res.*, **236**, 104811, https://doi.org/10.1016/j.atmosres.2019.104811.

Blumberg, W. G., K. T. Halbert, T. A. Supinie, P. T. Marsh, R. L. Thompson, and J. A. Hart, 2017: SHARPpy: An open-source sounding analysis toolkit for the atmospheric sciences. *Bull. Amer. Meteor. Soc.*, **98**, 1625–1636, https://doi.org/10.1175/BAMS-D-15-00309.1.

Bouwer, L. M., 2019: Observed and projected impacts from extreme weather events: Implications for loss and damage. *Loss and Damage from Climate Change*, R. Mechler et al., Eds., Climate Risk Management, Policy, and Governance, Springer, 63–82, https://doi.org/10.1007/978-3-319-72026-5_3.

Brooks, H. E., 2009: Proximity soundings for severe convection for Europe and the United States from reanalysis data. *Atmos. Res.*, **93**, 546–553, https://doi.org/10.1016/j.atmosres.2008.10.005.

——, and J. P. Craven, 2002: Database of proximity soundings for significant severe thunderstorms, 1957–1993. Preprints, *21st Conf. on Severe Local Storms*, San Antonio, TX, Amer. Meteor. Soc., 639–642.

——, and J. Correia Jr., 2018: Long-term performance metrics for National Weather Service tornado warnings. *Wea. Forecasting*, **33**, 1501–1511, https://doi.org/10.1175/WAF-D-18-0120.1.

——, J. W. Lee, and J. P. Craven, 2003: The spatial distribution of severe thunderstorm and tornado environments from global reanalysis data. *Atmos. Res.*, **67–68**, 73–94, https://doi.org/10.1016/S0169-8095(03)00045-0.

Brotzge, J., and W. Donner, 2013: The tornado warning process: A review of current research, challenges, and opportunities. *Bull. Amer. Meteor. Soc.*, **94**, 1715–1733, https://doi.org/10.1175/BAMS-D-12-00147.1.

Bruick, Z. S., K. L. Rasmussen, A. K. Rowe, and L. A. McMurdie, 2019: Characteristics of intense convection in subtropical South America as influenced by El Niño–Southern Oscillation. *Mon. Wea. Rev.*, **147**, 1947–1966, https://doi.org/10.1175/MWR-D-18-0342.1.

Bunkers, M. J., D. A. Barber, R. L. Thompson, R. Edwards, and J. Garner, 2014: Choosing a universal mean wind for supercell motion prediction. *J. Oper. Meteor.*, **2**, 115–129, https://doi.org/10.15191/nwajom.2014.0211.

Carbajal, N., J. F. León-Cruz, L. F. Pineda-Martínez, J. Tuxpan-Vargas, and J. H. Gaviño-Rodríguez, 2019: Occurrence of anticyclonic tornadoes in a topographically complex region of Mexico. *Adv. Meteor.*, **2019**, 2763153, https://doi.org/10.1155/2019/2763153.

Carvalho, L. M. V., C. Jones, and B. Liebmann, 2004: The South Atlantic convergence zone: Intensity, form, persistence, and relationships with intraseasonal to interannual activity and extreme rainfall. *J. Climate*, **17**, 88–108, https://doi.org/10.1175/1520-0442(2004)017<0088:TSACZI>2.0.CO;2.

Cecil, D. J., and C. B. Blankenship, 2012: Toward a global climatology of severe hailstorms as estimated by satellite passive microwave imagers. *J. Climate*, **25**, 687–703, https://doi.org/10.1175/JCLI-D-11-00130.1.

Coffer, B. E., and M. D. Parker, 2015: Impacts of increasing low-level shear on supercells during the early evening transition. *Mon. Wea. Rev.*, **143**, 1945–1969, https://doi.org/10.1175/MWR-D-14-00328.1.

——, ——, R. L. Thompson, B. T. Smith, and R. E. Jewell, 2019: Using near-ground storm relative helicity in supercell tornado forecasting. *Wea. Forecasting*, **34**, 1417–1435, https://doi.org/10.1175/WAF-D-19-0115.1.

——, M. Taszarek, and M. D. Parker, 2020: Near-ground wind profiles of tornadic and nontornadic environments in the United States and Europe from ERA5 reanalyses. *Wea. Forecasting*, **35**, 2621–2638, https://doi.org/10.1175/WAF-D-20-0153.1.

Craven, J. P., R. E. Jewell, and H. E. Brooks, 2002: Comparison between observed convective cloud-base heights and lifting condensation level for two different lifted parcels. *Wea. Forecasting*, **17**, 885–890, https://doi.org/10.1175/1520-0434(2002)017<0885:CBOCCB>2.0.CO;2.

Davis, J. M., and M. D. Parker, 2014: Radar climatology of tornadic and nontornadic vortices in high-shear, low-CAPE environments in the mid-Atlantic and southeastern United States. *Wea. Forecasting*, **29**, 828–853, https://doi.org/10.1175/WAF-D-13-00127.1.

DNM, 2002: Tornado in the department of Canelones (Uruguay), on March 10th, 2002 (in Spanish). DNM, 4 pp.

dos Santos, L. O., E. L. Nascimento, and J. T. Allen, 2023: Discriminant analysis for severe storm environments in south-central Brazil. *Mon. Wea. Rev.*, **151**, 2659–2681, https://doi.org/10.1175/MWR-D-22-0347.1.

Doswell, C. A., III, H. E. Brooks, and R. A. Maddox, 1996: Flash flood forecasting: An ingredients-based methodology. *Wea. Forecasting*, **11**, 560–581, https://doi.org/10.1175/1520-0434(1996)011<0560:FFFAIB>2.0.CO;2.

Durañona, V., 2016: Extreme wind climate of Uruguay. Ph.D. dissertation. Universidad de la Republica, 439 pp., https://www.colibri.udelar.edu.uy/jspui/handle/20.500.12008/8394.

Emanuel, K. A., 1994: *Atmospheric Convection*. Oxford University Press, 580 pp.

Fujita, T. T., 1971: Proposed characterization of tornadoes and hurricanes by area and intensity. SMRP Research Paper 91, University of Chicago, 42 pp., https://swco-ir.tdl.org/items/1bdb62ac-6f5d-4773-8d6f-ecaa06091ec9.

Gibbs, J. G., 2021: Evaluating precursor signals for QLCS tornado and higher impact straight-line wind events. *J. Oper. Meteor.*, **9**, 62–75, https://doi.org/10.15191/nwajom.2021.0905.

Goliger, A. M., and R. V. Milford, 1998: A review of worldwide occurrence of tornadoes. *J. Wind Eng. Ind. Aerodyn.*, **74–76**, 111–121, https://doi.org/10.1016/S0167-6105(98)00009-9.

Grams, J. S., R. L. Thompson, D. V. Snively, J. A. Prentice, G. M. Hodges, and L. J. Reames, 2012: A climatology and comparison of parameters for significant tornado events in the United States. *Wea. Forecasting*, **27**, 106–123, https://doi.org/10.1175/WAF-D-11-00008.1.

Grimm, A. M., 2019: Madden–Julian Oscillation impacts on South American summer monsoon season: Precipitation anomalies, extreme events, teleconnections, and role in the MJO cycle. *Climate Dyn.*, **53**, 907–932, https://doi.org/10.1007/s00382-019-04622-6.

——, and R. G. Tedeschi, 2009: ENSO and extreme rainfall events in South America. *J. Climate*, **22**, 1589–1609, https://doi.org/10.1175/2008JCLI2429.1.

Guyer, J. L., and A. R. Dean, 2010: Tornadoes within weak CAPE environments across the continental United States. Preprints, *25th Conf. on Severe Local Storms*, Denver, CO, Amer. Meteor. Soc., 1.5, https://ams.confex.com/ams/pdfpapers/175725.pdf.

Hamill, T. M., R. S. Schneider, H. E. Brooks, G. S. Forbes, H. B. Bluestein, M. Steinberg, D. Melendez, and R. M. Dole, 2005: The May 2003 extended tornado outbreak. *Bull. Amer. Meteor. Soc.*, **86**, 531–542, https://doi.org/10.1175/BAMS-86-4-531.

Hersbach, H., and Coauthors, 2020: The ERA5 global reanalysis. *Quart. J. Roy. Meteor. Soc.*, **146**, 1999–2049, https://doi.org/10.1002/qj.3803.

Houze, R. A., Jr., 2004: Mesoscale convective systems. *Rev. Geophys.*, **42**, RG4003, https://doi.org/10.1029/2004RG000150.

——, K. L. Rasmussen, M. D. Zuluaga, and S. R. Brodzik, 2015: The variable nature of convection in the tropics and subtropics: A legacy of 16 years of the Tropical Rainfall Measuring Mission satellite. *Rev. Geophys.*, **53**, 994–1021, https://doi.org/10.1002/2015RG000488.

IPCC, 2012: *Managing the Risks of Extreme Events and Disasters to Advance Climate Change Adaptation*. C. B. Field et al., Eds., Cambridge University Press, 582 pp.

Jorgensen, D. P., and T. M. Weckwerth, 2003: Forcing and organization of convective systems. *Radar and Atmospheric Science: A Collection of Essays in Honor of David Atlas*, *Meteor. Monogr.*, No. 30, Amer. Meteor. Soc., 75–103, https://doi.org/10.1175/0065-9401(2003)030<0075:FAOOCS>2.0.CO;2.

Kennedy, P. C., N. E. Westcott, and R. W. Scott, 1993: Single-Doppler radar observations of a mini-supercell tornadic

thunderstorm. *Mon. Wea. Rev.*, **121**, 1860–1870, https://doi.org/10.1175/1520-0493(1993)121<1860:SDROOA>2.0.CO;2.

Knapp, K. R., A. H. Young, H. Semunegus, A. K. Inamdar, and W. Hankins, 2021: Adjusting ISCCP cloud detection to increase consistency of cloud amount and reduce artifacts. *J. Atmos. Oceanic Technol.*, **38**, 155–165, https://doi.org/10.1175/JTECH-D-20-0045.1.

Knupp, K. R., and Coauthors, 2014: Meteorological overview of the devastating 27 April 2011 tornado outbreak. *Bull. Amer. Meteor. Soc.*, **95**, 1041–1062, https://doi.org/10.1175/BAMS-D-11-00229.1.

Liebmann, B., and C. A. Smith, 1996: Description of a complete (interpolated) outgoing longwave radiation dataset. *Bull. Amer. Meteor. Soc.*, **77**, 1275–1277, https://doi.org/10.1175/1520-0477-77.6.1274.

Lima, J. S., 1982: Analysis of a funnel-cloud occurrence in Santa Maria, Rio Grande do Sul: Application of a forecasting method (in Portuguese). *Proc. Second Brazilian Congress on Meteorology*, Pelotas, Brazil, Braz. Meteor. Soc., 382–392.

Liu, P., Q. Zhang, C. Zhang, Y. Zhu, M. Khairoutdinov, H.-M. Kim, C. Schumacher, and M. Zhang, 2016: A revised real-time multivariate MJO index. *Mon. Wea. Rev.*, **144**, 627–642, https://doi.org/10.1175/MWR-D-15-0237.1.

Lopes, M. M., 2020: Discriminando condições favoráveis a diferentes modos de tempo severo no leste da Bacia do Prata (in Portuguese). M.S. thesis, Dept. of Meteorology, Universidade Federal de Santa Maria, 122 pp., https://repositorio.ufsm.br/handle/1/22344?locale-attribute=pt_BR.

——, and E. L. Nascimento, 2020: Use of remote sensing via satellite in the identification of tornado damage paths in a severe weather event in Rio Grande do Sul. *Ciênc. Nat.*, **42**, e8, https://doi.org/10.5902/2179460X55309.

Maddox, R., 1976: An evaluation of tornado proximity wind and stability data. *Mon. Wea. Rev.*, **104**, 133–142, https://doi.org/10.1175/1520-0493(1976)104<0133:AEOTPW>2.0.CO;2.

Marengo, J. A., W. R. Soares, C. Saulo, and M. Nicolini, 2004: Climatology of the low-level jet east of the Andes as derived from the NCEP–NCAR reanalyses: Characteristics and temporal variability. *J. Climate*, **17**, 2261–2280, https://doi.org/10.1175/1520-0442(2004)017<2261:COTLJE>2.0.CO;2.

Markowski, P., C. Hannon, J. Frame, E. Lancaster, A. Pietrycha, R. Edwards, and R. L. Thompson, 2003: Characteristics of vertical wind profiles near supercells obtained from the rapid update cycle. *Wea. Forecasting*, **18**, 1262–1272, https://doi.org/10.1175/1520-0434(2003)018<1262:COVWPN>2.0.CO;2.

Markowski, P. M., and Y. P. Richardson, 2009: Tornadogenesis: Our current understanding, forecasting considerations, and questions to guide future research. *Atmos. Res.*, **93**, 3–10, https://doi.org/10.1016/j.atmosres.2008.09.015.

——, J. M. Straka, E. N. Rasmussen, and D. O. Blanchard, 1998: Variability of storm-relative helicity during VORTEX. *Mon. Wea. Rev.*, **126**, 2959–2971, https://doi.org/10.1175/1520-0493(1998)126<2959:VOSRHD>2.0.CO;2.

Mercer, A. E., C. M. Shafer, C. A. Doswell III, L. M. Leslie, and M. B. Richman, 2012: Objective classification of tornadic and nontornadic severe weather outbreaks. *Mon. Wea. Rev.*, **137**, 4355–4368, https://doi.org/10.1175/2009MWR2897.1.

Mo, K. C., and R. W. Higgins, 1998: The Pacific–South American modes and tropical convection during the Southern Hemisphere winter. *Mon. Wea. Rev.*, **126**, 1581–1596, https://doi.org/10.1175/1520-0493(1998)126<1581:TPSAMA>2.0.CO;2.

——, and J. N. Paegle, 2001: The Pacific-South American modes and their downstream effects. *Int. J. Climatol.*, **21**, 1211–1229, https://doi.org/10.1002/joc.685.

Montini, T. L., C. Jones, and L. M. V. Carvalho, 2019: The South American low-level jet: A new climatology, variability, and changes. *J. Geophys. Res. Atmos.*, **124**, 1200–1218, https://doi.org/10.1029/2018JD029634.

Mulholland, J. P., S. W. Nesbitt, R. J. Trapp, K. L. Rasmussen, and P. V. Salio, 2018: Convective storm life cycle and environments near the Sierras de Cordoba, Argentina. *Mon. Wea. Rev.*, **146**, 2541–2557, https://doi.org/10.1175/MWR-D-18-0081.1.

——, ——, and ——, 2019: A case study of terrain influences on upscale convective growth of a supercell. *Mon. Wea. Rev.*, **147**, 4305–4324, https://doi.org/10.1175/MWR-D-19-0099.1.

Nascimento, E. L., and C. A. Doswell III, 2006: The need for an improved documentation of severe thunderstorms and tornadoes in South America. *Symp. Challenges of Severe Convective Storms*, Atlanta, GA, Amer. Meteor. Soc., P1.18, https://ams.confex.com/ams/Annual2006/techprogram/paper_102247.htm.

——, G. Held, and A. M. Gomes, 2014: A multiple-vortex tornado in southeastern Brazil. *Mon. Wea. Rev.*, **142**, 3017–3037, https://doi.org/10.1175/MWR-D-13-00319.1.

Nascimento, M. G., D. L. Herdies, and D. Oliveira de Souza, 2016: The South American water balance: The influence of low-level jets. *J. Climate*, **29**, 1429–1449, https://doi.org/10.1175/JCLI-D-15-0065.1.

Natalini, B., J. L. Lassig, M. B. Natalini, and C. Palese, 2012: Wind-induced damage in two regions of Argentina. *J. Civ. Eng. Archit.*, **6**, 167, https://doi.org/10.17265/1934-7359/2012.02.004.

Nesbitt, S. W., and Coauthors, 2021: A storm safari in subtropical South America: Proyecto RELAMPAGO. *Bull. Amer. Meteor. Soc.*, **102**, E1621–E1644, https://doi.org/10.1175/BAMS-D-20-0029.1.

Nouri, N., N. Devineni, V. Were, and R. Khanbilvardi, 2021: Explaining the trends and variability in the United States tornado records using climate teleconnections and shifts in observational practices. *Sci. Rep.*, **11**, 1741, https://doi.org/10.1038/s41598-021-81143-5.

Nunes, L. H., L. De Bona, and D. H. Candido, 2011: Tornado and waterspout climatology in Brazil. *Sixth European Conf. on Severe Storms (ECSS 2011)*, Palma de Mallorca, Spain, European Severe Storms Laboratory, 3 pp., https://citeseerx.ist.psu.edu/viewdoc/download?doi=10.1.1.686.9041&rep=rep1&type=pdf.

Oliveira, I. P. V., 2004: Analysis of tornado events in Santa Catarina (Brazil): Synoptic characterization and evaluation of data (in Portuguese). INPE—National Institute of Space Research, 225 pp.

Oliveira, M. I., F. S. Puhales, E. L. Nascimento, and V. Anabor, 2022: Integrated damage, visual, remote sensing, and environmental analysis of a strong tornado in southern Brazil. *Atmos. Res.*, **274**, 106188, https://doi.org/10.1016/j.atmosres.2022.106188.

Ortiz-Royero, J. C., and M. Rosales, 2012: Severe tornadoes on the Caribbean coast of Colombia since 2001 and their relation to local climate conditions. *Nat. Hazards*, **64**, 1805–1821, https://doi.org/10.1007/s11069-012-0337-8.

Parker, M. D., 2014: Composite VORTEX2 supercell environments from near-storm soundings. *Mon. Wea. Rev.*, **142**, 508–529, https://doi.org/10.1175/MWR-D-13-00167.1.

Pereira Filho, A. J., F. Vemado, and H. A. Karam, 2019: Evidence of tornadoes and microbursts in Sao Paulo State, Brazil: A

synoptic and mesoscale analysis. *Pure Appl. Geophys.*, **176**, 5079–5106, https://doi.org/10.1007/s00024-019-02276-3.

Piersante, J. O., K. L. Rasmussen, R. S. Schumacher, A. K. Rowe, and L. A. McMurdie, 2021: A synoptic evolution comparison of the smallest and largest MCSs in subtropical South America between spring and summer. *Mon. Wea. Rev.*, **149**, 1943–1966, https://doi.org/10.1175/MWR-D-20-0208.1.

Pita, G. L., and M. L. A. Schwarzkopf, 2016: Urban downburst vulnerability and damage assessment from a case study in Argentina. *Nat. Hazards*, **83**, 445–463, https://doi.org/10.1007/s11069-016-2323-z.

Potvin, C. K., C. Broyles, P. S. Skinner, and H. E. Brooks, 2022: Improving estimates of U.S. tornado frequency by accounting for unreported and underrated tornadoes. *J. Appl. Meteor. Climatol.*, **61**, 909–930, https://doi.org/10.1175/JAMC-D-21-0225.1.

Rasmussen, E. N., and D. O. Blanchard, 1998: A baseline climatology of sounding-derived supercell and tornado forecast parameters. *Wea. Forecasting*, **13**, 1148–1164, https://doi.org/10.1175/1520-0434(1998)013<1148:ABCOSD>2.0.CO;2.

Rasmussen, K. L., and R. A. Houze Jr., 2011: Orogenic convection in subtropical South America as seen by the TRMM satellite. *Mon. Wea. Rev.*, **139**, 2399–2420, https://doi.org/10.1175/MWR-D-10-05006.1.

——, and ——, 2016: Convective initiation near the Andes in subtropical South America. *Mon. Wea. Rev.*, **144**, 2351–2374, https://doi.org/10.1175/MWR-D-15-0058.1.

——, M. D. Zuluaga, and R. A. Houze Jr., 2014: Severe convection and lightning in subtropical South America. *Geophys. Res. Lett.*, **41**, 7359–7366, https://doi.org/10.1002/2014GL061767.

——, M. M. Chaplin, M. D. Zuluaga, and R. A. Houze Jr., 2016: Contribution of extreme convective storms to rainfall in South America. *J. Hydrometeor.*, **17**, 353–367, https://doi.org/10.1175/JHM-D-15-0067.1.

Ray, P. S., P. Bieringer, X. Niu, and B. Whissel, 2003: An improved estimate of tornado occurrence in the central plains of the United States. *Mon. Wea. Rev.*, **131**, 1026–1031, https://doi.org/10.1175/1520-0493(2003)131<1026:AIEOTO>2.0.CO;2.

Rehbein, A., and Coauthors, 2018: Severe weather events over southeastern Brazil during the 2016 dry season. *Adv. Meteor.*, **2018**, 4878503, https://doi.org/10.1155/2018/4878503.

Ribeiro, B. Z., and L. F. Bosart, 2018: Elevated mixed layers and associated severe thunderstorm environments in south and North America. *Mon. Wea. Rev.*, **146**, 3–28, https://doi.org/10.1175/MWR-D-17-0121.1.

Rocque, M. N., and K. L. Rasmussen, 2022: The impact of topography on the environment and life cycle of weakly and strongly forced MCSs during RELAMPAGO. *Mon. Wea. Rev.*, **150**, 2317–2338, https://doi.org/10.1175/MWR-D-22-0049.1.

Sasaki, C., A. K. Rowe, L. A. Mcmurdie, and K. L. Rasmussen, 2022: New insights into the South American low-level jet from RELAMPAGO observations. *Mon. Wea. Rev.*, **150**, 1247–1271, https://doi.org/10.1175/MWR-D-21-0161.1.

Schumacher, R. S., and K. L. Rasmussen, 2020: The formation, character and changing nature of mesoscale convective systems. *Nat. Rev. Earth Environ.*, **1**, 300–314, https://doi.org/10.1038/s43017-020-0057-7.

——, and Coauthors, 2021: Convective-storm environments in subtropical South America from high-frequency soundings during RELAMPAGO-CACTI. *Mon. Wea. Rev.*, **149**, 1439–1458, https://doi.org/10.1175/MWR-D-20-0293.1.

Schwarzkopf, M. L. A., 1988: Climatology of the effects of severe convection over Argentina (in Spanish). Ph.D. dissertation, Universidad de Buenos Aires, 91 pp., https://bibliotecadigital.exactas.uba.ar/download/tesis/tesis_n2211_AltingerdeSchwarzkopf.pdf.

——, and L. C. Rosso, 1993: Risk of tornadoes and downbursts in Argentina (in Spanish). Dept. of Atmospheric Sciences, School of Exact and Natural Sciences, Universidad de Buenos Aires, 35 pp.

Sena, A. C. T., Y. Peings, and G. Magnusdottir, 2022: Effect of the Quasi-Biennial Oscillation on the Madden Julian Oscillation teleconnections in the Southern Hemisphere. *Geophys. Res. Lett.*, **49**, e2021GL096105, https://doi.org/10.1029/2021GL096105.

Sherburn, K. D., and M. D. Parker, 2014: Climatology and ingredients of significant severe convection in high-shear, low-CAPE environments. *Wea. Forecasting*, **29**, 854–877, https://doi.org/10.1175/WAF-D-13-00041.1.

——, ——, J. R. King, and G. M. Lackmann, 2016: Composite environments of severe and nonsevere high-shear, low-CAPE convective events. *Wea. Forecasting*, **31**, 1899–1927, https://doi.org/10.1175/WAF-D-16-0086.1.

Silva, G. A. M., and T. Ambrizzi, 2006: Inter-El Niño variability and its impact on the South American low-level jet east of the Andes during austral summer—Two case studies. *Adv. Geosci.*, **6**, 283–287, https://doi.org/10.5194/adgeo-6-283-2006.

Silva Dias, M. A. F., 2011: An increase in the number of tornado reports in Brazil. *Wea. Climate Soc.*, **3**, 209–217, https://doi.org/10.1175/2011WCAS1095.1.

Smith, B. T., R. L. Thompson, J. S. Grams, C. Broyles, and H. E. Brooks, 2012: Convective modes for significant severe thunderstorms in the contiguous United States. Part I: Storm classification and climatology. *Wea. Forecasting*, **27**, 1114–1135, https://doi.org/10.1175/WAF-D-11-00115.1.

Straub, K. H., 2013: MJO initiation in the real-time multivariate MJO index. *J. Climate*, **26**, 1130–1151, https://doi.org/10.1175/JCLI-D-12-00074.1.

Swain, D. L., O. E. J. Wing, P. D. Bates, J. M. Done, K. A. Johnson, and D. R. Cameron, 2020: Increased flood exposure due to climate change and population growth in the United States. *Earth's Future*, **8**, e2020EF001778, https://doi.org/10.1029/2020EF001778.

Taszarek, M., J. T. Allen, T. Púčik, K. A. Hoogewind, and H. E. Brooks, 2020: Severe convective storms across Europe and the United States. Part II: ERA5 environments associated with lightning, large hail, severe wind, and tornadoes. *J. Climate*, **33**, 10 263–10 286, https://doi.org/10.1175/JCLI-D-20-0346.1.

——, N. Pilguj, J. T. Allen, V. Gensini, H. E. Brooks, and P. Szuster, 2021: Comparison of convective parameters derived from ERA5 and MERRA-2 with rawinsonde data over Europe and North America. *J. Climate*, **34**, 3211–3237, https://doi.org/10.1175/JCLI-D-20-0484.1.

Thompson, D. B., and P. E. Roundy, 2013: The relationship between the Madden–Julian Oscillation and U.S. violent tornado outbreaks in the spring. *Mon. Wea. Rev.*, **141**, 2087–2095, https://doi.org/10.1175/MWR-D-12-00173.1.

Thompson, R. L., R. Edwards, J. A. Hart, K. L. Elmore, and P. Markowski, 2003: Close proximity soundings within supercell environments obtained from the Rapid Update Cycle. *Wea. Forecasting*, **18**, 1243–1261, https://doi.org/10.1175/1520-0434(2003)018<1243:CPSWSE>2.0.CO;2.

——, ——, and C. M. Mead, 2004: An update to the supercell composite and significant tornado parameters. *22nd Conf. on Severe Local Storms*, Hyannis, MA, Amer. Meteor. Soc.,

P8.1, https://ams.confex.com/ams/11aram22sls/techprogram/paper_82100.htm.

——, B. T. Smith, J. S. Grams, A. R. Dean, and C. Broyles, 2012: Convective modes for significant severe thunderstorms in the contiguous United States. Part II: Supercell and QLCS tornado environments. *Wea. Forecasting*, **27**, 1136–1154, https://doi.org/10.1175/WAF-D-11-00116.1.

Tippett, M. K., 2018: Robustness of relations between the MJO and U.S. tornado occurrence. *Mon. Wea. Rev.*, **146**, 3873–3884, https://doi.org/10.1175/MWR-D-18-0207.1.

Tochimoto, E., 2022: Environmental controls on tornadoes and tornado outbreaks. *Atmos.–Ocean*, **60**, 399–421, https://doi.org/10.1080/07055900.2022.2079472.

Trapp, R. J., D. M. Wheatley, N. T. Atkins, R. W. Przybylinksi, and R. Wolf, 2006: Buyer beware: Some words of caution on the use of severe wind reports in postevent assessment and research. *Wea. Forecasting*, **21**, 408–415, https://doi.org/10.1175/WAF925.1.

Tuholske, C., K. Caylor, C. Funk, A. Verdin, S. Sweeney, K. Grace, P. Peterson, and T. Evans, 2021: Global urban population exposure to extreme heat. *Proc. Natl. Acad. Sci. USA*, **118**, e2024792118, https://doi.org/10.1073/pnas.2024792118.

Varga, Á. J., and H. Breuer, 2022: Evaluation of convective parameters derived from pressure level and native ERA5 data and different resolution WRF climate simulations over central Europe. *Climate Dyn.*, **58**, 1569–1585, https://doi.org/10.1007/s00382-021-05979-3.

Veloso-Aguila, D., 2023: Tornado reports in southeast South America (version 2). Zenodo, accessed 14 December 2023, https://doi.org/10.5281/zenodo.7072781.

Vera, C., and Coauthors, 2006: The South American low-level jet experiment. *Bull. Amer. Meteor. Soc.*, **87**, 63–77, https://doi.org/10.1175/BAMS-87-1-63.

Vicencio, J., and Coauthors, 2021: The Chilean tornado outbreak of May 2019: Synoptic, mesoscale, and historical contexts. *Bull. Amer. Meteor. Soc.*, **102**, E611–E634, https://doi.org/10.1175/BAMS-D-19-0218.1.

Wheeler, M. C., and H. H. Hendon, 2004: An all-season real-time multivariate MJO index: Development of an index for monitoring and prediction. *Mon. Wea. Rev.*, **132**, 1917–1932, https://doi.org/10.1175/1520-0493(2004)132<1917:AARMMI>2.0.CO;2.

Yang, J., L. Hu, and C. Wang, 2019: Population dynamics modify urban residents' exposure to extreme temperatures across the United States. *Sci. Adv.*, **5**, eaay3452, https://doi.org/10.1126/sciadv.aay3452.

Young, A. H., K. R. Knapp, A. Inamdar, W. Hankins, and W. B. Rossow, 2018: The international satellite cloud climatology project H-Series climate data record product. *Earth Syst. Sci. Data*, **10**, 583–593, https://doi.org/10.5194/essd-10-583-2018.

Zipser, E. J., D. J. Cecil, C. Liu, S. W. Nesbitt, and D. P. Yorty, 2006: Where are the most intense thunderstorms on Earth? *Bull. Amer. Meteor. Soc.*, **87**, 1057–1072, https://doi.org/10.1175/BAMS-87-8-1057.